Journal of Materials Chemistry A

ROYAL SOCIETY OF CHEMISTRY

PAPER

Published on 13 May 2025
Licence and permissions

Check for updates

Cite this: J. Mater. Chem. A, 2025, 13, 19795

Unveiling the effect of structural asymmetry on photocatalytic performance: Bi-substituted $Y_2Sn_2O_7$ system with mechanistic insight†

Adarsh Kumar,[ab] Deepak Tyagi,[ab] Ravi Kumar,[c] Manasi Ghosh,[d] Balaji P. Mandal,[ab] Ahin Roy,[e] Sukhendu Nath,[bf] Avesh K. Tyagi *[b] and Kaustava Bhattacharyya *[ab]

Received 3rd March 2025
Accepted 6th May 2025

DOI: 10.1039/d5ta01746g

rsc.li/materials-a

This study investigated the impact of structural distortion on the photocatalytic activity of Bi-substituted $Y_2Sn_2O_7$. By tuning the electronic structure of $Y_2Sn_2O_7$ through Bi substitution, its charge carrier (electron–hole pair, e^-/h^+) dynamics, including surface transfer, lifetime, and recombination pathways, were modulated. A series of Bi-substituted $Y_2Sn_2O_7$ photocatalysts was synthesized and thoroughly characterized. Subsequently, their photocatalytic performance was evaluated by degrading *para*-chlorophenol (*p*-CP) (one of the major synthons of dioxins and furans) under UV and visible light irradiation. Our findings revealed a strong correlation between photocatalytic activity and different structural factors, such as the bandgap, flat band potential, and surface charge. In-depth XPS and EPR analysis highlighted the influence of oxygen vacancies on charge carrier trapping within the pyrochlore/tetragonal structures. Furthermore, it was demonstrated that the structural asymmetry of Bi-substituted $Y_2Sn_2O_7$ significantly impacted its photocatalytic efficiency *via* the formation of various intermediates during the photo-oxidation of *p*-CP and their mechanistic roles. Finally, femtosecond dynamics studies provided insights into the dominant role of either holes (h^+) or alternative pathways in the photo-oxidation process. This work provides a comprehensive understanding of the interplay among the structural parameters, electronic properties, and photocatalytic activity of Bi-substituted $Y_2Sn_2O_7$ systems.

1. Introduction

In the realm of photocatalysis, photocatalysts with lower symmetry are typically correlated with an indirect band gap, although the band gap itself is not solely linked to long-range ordering. Short-range properties also significantly influence band gap engineering. Thus, to investigate the impact of structural asymmetry on photocatalytic properties, starting with

[a]Chemistry Division, Bhabha Atomic Research Centre, Mumbai 40085, India. E-mail: kaustava@barc.gov.in

[b]Homi Bhabha National Institute, Mumbai 400 094, India. E-mail: aktyagi@barc.gov.in

[c]Atomic and Molecular Physics Division, Bhabha Atomic Research Centre, Mumbai 400 085, India

[d]Physics Section, MMV, Banaras Hindu University, Varanasi 221005, India

[e]Materials Science Centre, Indian Institute of Technology Kharagpur, West Bengal 721302, India

[f]Radiation and Photochemistry Division, Bhabha Atomic Research Centre, Mumbai 40085, India

† Electronic supplementary information (ESI) available: UV-vis data (Fig. S.1–S.7): Fig. S.1(a) and (b): shows the UV-vis data for the self-degradation of *p*-CP under visible light and UV light. (Fig. S.2–S.7) Depict the degradation of *p*-CP using various photocatalysts (BSN, $Y_{0.4}Bi_{1.6}Sn_2O_7$, *etc.*) as a function of time. FT-IR spectroscopy (Fig. S.8): IR data of liquid *p*-CP and *p*-CP over KBr. Table S.1 assigns the different bands observed in the spectrum. (Fig. S.9–S.11) Represent FT-IR spectra for the adsorption of *p*-CP on different photocatalysts (YSN, BSN, $Y_{0.1}Bi_{1.9}Sn_2O_7$ and $Y_{0.3}Bi_{1.7}Sn_2O_7$) across various vibrational ranges. Schemes 1–3 depict the corresponding adsorption processes. X-ray photoelectron spectroscopy (XPS) and X-ray absorption spectroscopy (XAS) (Fig. S.12–S.16): Fig. S.13: XPS data for Y 3p with deconvolution into $3p_{3/2}$ and $3p_{1/2}$ for the various samples. Fig. S.14: represents normalized XAS spectra of $Y_{2-x}Bi_xSn_2O_7$ samples at the Sn K edge. Fig. S.15–S.17: depict EXAFS ($k^2\chi(k)$ *vs.* k) spectra of $Y_{2-x}Bi_xSn_2O_7$ samples at the Sn K edge, Y K edge, and Bi L_3 edge, respectively (Fig. S.17–S.24 and Tables S.2–S.4): Table S.2: provides the calculated apparent quantum efficiencies of the different photocatalysts. Fig. S.17: DR-UV-vis spectra for the $Y_{2-x}Bi_xSn_2O_7$ samples. Fig. S.18: shows transient absorption spectra of water-dispersed BSN in the presence of triethanolamine (TEOH) at different delay times, along with the decay kinetics of the transient at 1070 nm. Fig. S.19 and S.20: represent transient decay kinetics recorded at 860 nm and 1070 nm for a water-dispersed BSN solution. Fig. S.21: the complete-oxidation of *p*-CP under visible irradiation and the product being studied by mass spectroscopy. Fig. S.22: TGA study of the different sets of catalysts. Table S.3: chemical shift anisotropy (CSA) parameter. Fig. S.23: ^{119}Sn MAS SSNMR spectra of different catalysts at magic angle spinning (MAS). Fig. S.24–S.27: degradation of *p*-CP in acidic solution, basic solution, and H_2O_2 as well as in the presence of a hole quencher (triethyl amine) and radical scavengers using the BSN photocatalyst as a function of time. Fig. S.28(A). XRD of BSN: (a) as-synthesised and (b) post-catalytic treatment; Fig. S.28(B): survey scans of the BSN and BSN after photocatalytic irradiation. Table S.4: elemental composition of the BSN photocatalyst from XPS before and after photo-irradiation. See DOI: https://doi.org/10.1039/d5ta01746g

a cubic pyrochlore and transitioning to lower symmetry structures become an intriguing possibility. Materials with an ideal pyrochlore structure and crystallizing in the $Fd\bar{3}m$ space group have the general formula $A_2B_2O_6O'$, where A-site cations (generally 2^+ or 3^+) have a coordination number of 8, B-site cations (generally 4^+ or 5^+) have a coordination number of 6, O anions occupy the 48f sites, and O′ anions occupy 8a sites.[1] They have been widely studied for various applications requiring different properties such as ferroelectricity,[2] dielectric properties,[3] CO sensing,[4] spin-ice magnetic frustration[5] and photocatalysis.[6] A-site cations (usually possessing an ionic radius of ~1 Å) are typically scalenohedral (distorted cubes) containing six equally spaced anions (O atoms) and two at a slightly shorter distance from the central cation, and smaller B-site cations (ionic radius of ~0.6 Å) have a trigonal antiprismatic structure (distorted octahedra) with six anions at an equal distance from the central cation. The stability of the pyrochlore structure strongly depends on the ratio of the radius of the A- to B-site cations (r_A/r_B). If this ratio exceeds 1.78, the ordered pyrochlore structure is transformed to a monoclinic structure, whereas for a radius ratio below 1.46, it forms a disordered, defect-fluorite structure.[7] Previous studies have shown that A-site cations usually regulate the size and charge,[8] electronic configuration and valence band properties.[9] B-site cations mainly regulate the coordination environment,[10] electronic configuration[11] and conduction band properties.[12] The lone pair in the A site can induce structural distortions and enhance ferroelectricity or photocatalytic activity.[13] Different properties such as photocatalysis, ionic conductivity, dielectric properties, disordering, electronic properties, magnetic frustration and exotic phases, thermal conductivity and radiation damage are altered by different constitutions of A and B cations.

Currently, pyrochlores have attracted increasing interest (typically $A_2B_2O_7$ structure with a coordination number of A-8 and B-6), where Bi(III) occupies the A-site. This placement strategically displaces the stereochemically active Bi-lone pair from its usual highly symmetrical, high coordination environment[14] to a one with lower symmetry and coordination. $Bi_2Sn_2O_7$ (BSN) was described as a pyrochlore-related structure, exhibiting a distinct diffraction pattern, which cannot be directly indexed as a cubic system. Subsequently, the meticulous temperature-dependent investigations by Shannon *et al.*[15] revealed the existence of three distinct BSN polymorphs, *i.e.*, α-monoclinic, β-face-centred cubic, and γ-cubic. Among them, the γ-cubic phase, embodying the pyrochlore structure, possesses a considerably dispersed valence band characterized by hybridized Bi $6s^26p^0$ and Sn $5s^05p^0$ states, together with a minor contribution from O 2p. This configuration gives rise to a deeply situated valence band state, which in turn facilitates the charge carrier mobility. This, coupled with its narrow band gap, generally translates to the efficient utilization of electron–hole pairs, making γ-cubic BSN a compelling photocatalyst in the visible light spectrum.[16] The dispersed nature of the s and p-orbitals, owing to their low effective masses of electrons and holes (e^-/h^+), further bolsters the photocatalytic efficacy by enabling their facile transport to the surface.[17] In recent times, this type of material has been harnessed as a photocatalyst by numerous research groups, either directly or in the form of heterojunctions capitalizing on the low band gap of BSN.[18] However, the impact of the structure of α-monoclinic BSN on its photocatalytic properties remains elusive, primarily due to the inherent difficulty in precisely determining its structure, which consists of 176 crystallographically unique atoms. Thus, to gain a deeper understanding of how the structure of these asymmetric configurations influences their catalytic properties, a strategic approach is starting with a symmetrical structure and progressively introducing asymmetry. Subsequently, by systematically observing the ensuing modifications in their photocatalytic behaviour, we can elucidate their structure–property relationship. Notably, both bismuth and yttrium-substituted tin oxide pyrochlores have been demonstrated to exhibit exceptional photocatalytic activity when irradiated with visible light.[19] The photocatalytic properties of Bi-based structures have been well studied recently for several redox reactions.[20–23] Chloro-phenols (CPs) have garnered significant attention from environmental regulatory bodies due to their inclusion in the priority pollutant lists of several Environmental Protection Agencies.[24–26] To date, numerous treatment techniques such as adsorption, biodegradation, electrochemical reduction and Fenton-like advanced oxidation processes[27–31] have been explored for the treatment of CPs. However, their implementation is often hampered by cost considerations stemming from the use of excessive oxidants, substantial energy requirements, and strict conditions.[32,33] Furthermore, the transformation of *para*-chlorophenol, a precursor for dioxins and furans, necessitates an environmentally benign approach. In this context, visible light-driven photocatalytic degradation has emerged as a particularly attractive strategy for directly mitigating CPs. However, conventional photocatalysts such as TiO_2 and SnO_2 exhibit temperature-dependent phase transitions, which compromise their photocatalytic efficacy. Furthermore, the mechanistic understanding of the photocatalytic degradation of chloro-phenols has still not been completely established and requires a more standard understanding.[34] Thus, to address this limitation, pyrochlores, which are well-known for their exceptional structural integrity, present a compelling alternative.

The present work delved into the intriguing interplay between structural asymmetry and photocatalytic activity in pyrochlores. $Y_2Sn_2O_7$ (YSN), a prototypical pyrochlore with a UV-region band gap, served as the foundation for this investigation. Through strategic Bi-substitution, the YSN lattice was manipulated to induce a transition towards a more asymmetric tetragonal structure, leading to a visible light-absorbing band gap. By systematically studying the photocatalytic properties of asymmetric BSN, achieved through Bi substitution in the YSN lattice, the pivotal role of asymmetry in apparent quantum efficiency was revealed. The identification of different intermediates formed on the surface of the catalyst during the visible light-driven photocatalytic degradation process revealed the catalytic route, which can be used to understand the complete kinetics of this system. Femtosecond chemistry was employed to ascertain whether the degradation mechanism involves a direct hole-mediated reaction.

2. Experimental

2.1. Catalyst synthesis

The catalysts were synthesized *via* the co-precipitation method (Scheme 1). Bismuth nitrate pentahydrate [$Bi(NO_3)_3 \cdot 5H_2O$], yttrium oxide (Y_2O_3) and tin chloride ($SnCl_4$) were used as the precursors and added in a stoichiometric ratio to deionised water in a beaker and stirred for 2 h.

Ammonium hydroxide was added to the solution until the pH reached 11. The resulting precipitates were filtered, extensively washed with water, and subsequently with methanol. Then, the precipitates were dried overnight at 90 °C. The solid mass obtained was heated at 750 °C for 10 h in an ambient atmosphere and utilized for subsequent experiments. The process involved Bi-substitution in the YSN lattice, denoted as $Y_{2-x}Bi_xSn_2O_7$ (x = 0, 1.6, 1.7, 1.8, 1.9, 2). Herein, x = 0, *i.e.* $Y_2Sn_2O_7$, is referred to as YSN and x = 2, *i.e.* $Bi_2Sn_2O_7$, is termed BSN.

2.2. Characterization

The different characterization techniques included crystallography, DRS-UV-vis spectroscopy, Raman spectroscopy, morphological study, X-ray photoelectron spectroscopy (XPS), X-ray absorption spectroscopy (EXAFS and XANES), surface area analysis, zeta potential, and EPR. The details are described in the ESI [Page No. 1–3].†

2.3. Photo-electrochemical measurements

The Mott–Schottky and photovoltaic switching experiments are described in detail in the ESI (Page No. 4).†

2.4. Photocatalytic activity

The photo-catalytic efficacy of different substituted catalysts was assessed using a spectrophotometer, employing $Y_xBi_{2-x}Sn_2O_7$ (x = 0–2.0) pyrochlore/pyrochlore type in experimental investigations. The calculated low effective masses of charge carriers and favourable band edge positions affirm the photocatalytic potential of these pyrochlores. The experimental setup involved confining the reactants in a cylindrical Pyrex glass reactor, which was irradiated either with a 400 W medium-pressure Hg lamp (flux = 170 mW cm^{-2}) positioned perpendicularly in the reactor, or with a white light source emitting in the 350–750 nm range (flux = 234 mW cm^{-2}) with a peak around 430 nm. The photon flux, measured using a uranyl oxalate actinometer, was approximately ~6.5 × 10^{14} photons per cm^2 per s. The photo-degradation reaction utilized an aqueous solution of *para*-chlorophenol (*p*-CP) as a model degradable substance, with pyrochlore powders acting as photocatalysts.

In the photo-degradation reaction, 100 mg of a photocatalyst sample was introduced into a 60 mL *p*-CP solution with a molar concentration of 3.3 × 10^{-5} mol dm^{-3}. Stirring the photocatalytic systems for 5 min at 200 rpm facilitated the dispersion of powders, considering that pyrochlores are partially soluble in an aqueous medium. Subsequently, the systems were exposed to visible light, and at every 10 min interval, one system was withdrawn for absorbance measurement using an ultraviolet-visible (UV-vis) spectrophotometer. Post each measurement, the mixtures underwent an additional 10 min of stirring. The optical absorption measurement of the supernatant was carried out on a JASCO UV-670 spectrophotometer at the wavelength of λ = 225 nm, corresponding to the absorption maximum for the

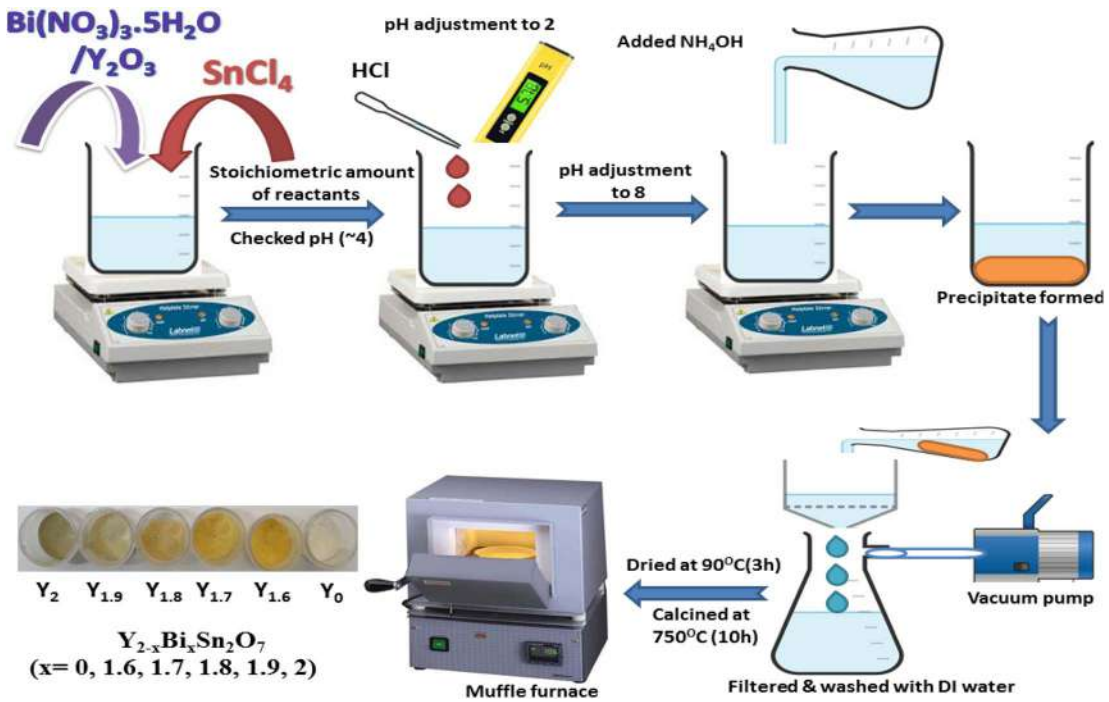

Scheme 1 Synthesis of crystalline $Y_{2-x}Bi_xSn_2O_7$ (x = 0, 1.6, 1.7, 1.8, 1.9, and 2) *via* the co-precipitation method.

p-CP solution. The evaluation of photocatalytic activity was performed thrice to ensure repeatability.

2.5. *Ex situ* FTIR studies

The intermediates were studied using *ex situ* FT-IR and the details of these experiments are described in the ESI [Page No. 4 and 5].†

2.6. Femtosecond transient absorption (FTAS) and time-resolved photoluminescence experiments (TRPL)

The details of the time-resolved photoluminescence (TRPL) and femtosecond transient absorption (FTAS) experiments are discussed in the ESI (Page No. 5).†

3. Results and discussion

3.1. X-ray diffraction (XRD)

Ideal pyrochlores adopt a cubic structure with just four crystallographically independent atoms. They crystallize in the $Fd\bar{3}m$ space group, with the A-site cation on the 16c site, B-site cation on the 16d site and oxygens on the 48f and 8a sites (the latter is often referred to as O′).[35] The bulk YSN unit cell exhibits a defective fluorite lattice with the alternating placement of Y^{3+} and Sn^{4+} ions in an FCC structure, where $1/8^{th}$ of the anion sites remain vacant. The Y^{3+} ions reside at the 16d (Wyckoff notation) sites, each surrounded by eight oxygen atoms in a scalenohedral geometry. The Sn^{4+} ions, located at the 16c sites, are coordinated with six oxygen atoms. The structural network is comprised of YO_8 cubic-polyhedra and SnO_6 octahedra. In the YO_8 polyhedra, two oxygen atoms correspond to 8b crystallographic symmetry,[31] while the remaining six correspond to 48f. The SnO_6 polyhedra involve all six oxygen atoms from the 48f crystallographic site. In contrast to α-BSN, where Bi has a coordination number of 5 and Sn exhibits an octahedral coordination, YSN is a cubic pyrochlore with the $Fd\bar{3}m$ space group and O_{h7} point group. BiO_5 is attached to SnO_6 by only corner sharing (Scheme 2) and few edge sharing, forming a very complex structure, as has been hypothesised by many groups recently, where the unit cell is comprised of 176 atoms.[7,36]

The XRD patterns of the compounds indicate that all the compositions are single phasic in nature. YSN was found to have pyrochlore ordering, which is characterized by the presence of typical super-lattice peaks at 2θ values of 14°, 27°, and 45° (using Cu-Kα radiation source), corresponding to (111), (311), and (511), respectively (Fig. 1A(a)). The XRD patterns in (Fig. 1A) reveal that the structure closely resembles a cubic pyrochlore, with prominent pyrochlore peaks for YSN. The structure of BSN is intricate, showing smaller peaks, which indicate a less symmetric α- or β-polymorph.

Shannon *et al.* reported that α-BSN transforms to β-BSN above 410 K.[15] The peaks at 14.4°, 23.6°, 24.66°, 27.76°, and 36.6° suggest the formation of the tetragonal BSN phase (α form) at room temperature.[37] An increase in the Y content in the composition shifted the XRD peaks to higher angles, indicating decreased cell parameters. Beyond Y substitution ($x \geq 1.6$) in $Y_{2-x}Bi_xSn_2O_7$, the system became biphasic with cubic YSN peaks.[38] Bi-substituted YSN structures closely resemble tetragonal BSN,[39] differing from the YSN pyrochlore structure. Considering the system as Y-substituted BSN, the lattice parameters contract ($a = b$), reducing the unit cell volume.[40] YSN, being a symmetric cubic structure ($a = b = c$), exhibits a further reduced unit cell volume due to the significant reduction in the lattice parameter in the *z*-axis. The crystallite size, calculated using the Williamson–Hall equation (eqn (1)) after subtraction of the strain part, remained ~24 nm for all the materials sintered at 750 °C for an extended period.

The contribution from the crystallite size and strain could be delineated using the Williamson–Hall equation (eqn (1)).

$$B\cos\theta = 0.9\lambda/t + \eta\sin\theta \quad (1)$$

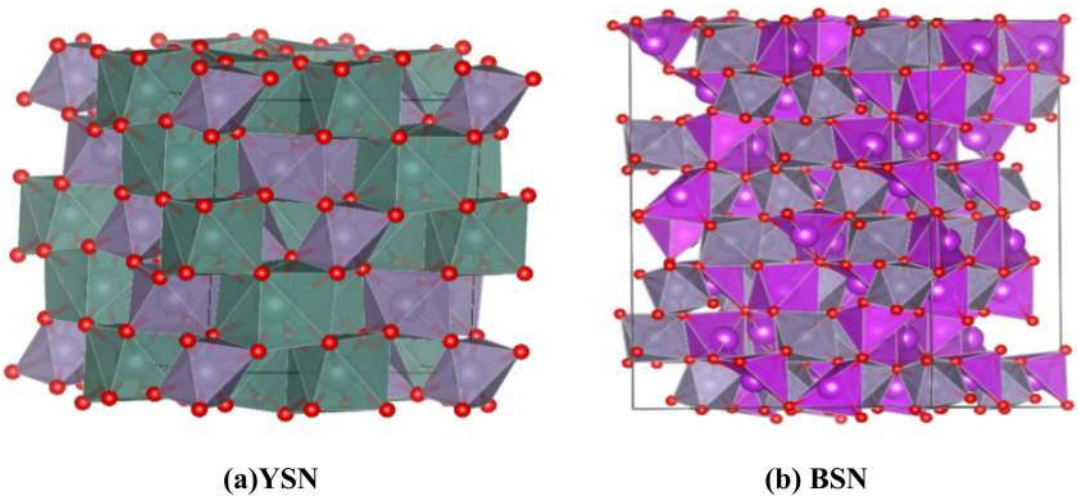

Scheme 2 Schematic representation of (a) the polyhedral YSN structure of YSN with the required cubic YO_8 polyhedra and SnO_6 octahedra. (b) Polyhedral BSN structure of YSN with the required cubic BO_5 polyhedra and SnO_6 octahedra. Red balls: oxygen (O) atoms (in YSN and BSN). Green balls (in YSN): yttrium (Y) atoms. Purple balls (in YSN): tin (Sn) atoms. Magenta balls (in BSN): bismuth (Bi) atoms. Purple balls (in BSN): tin (Sn) atoms.

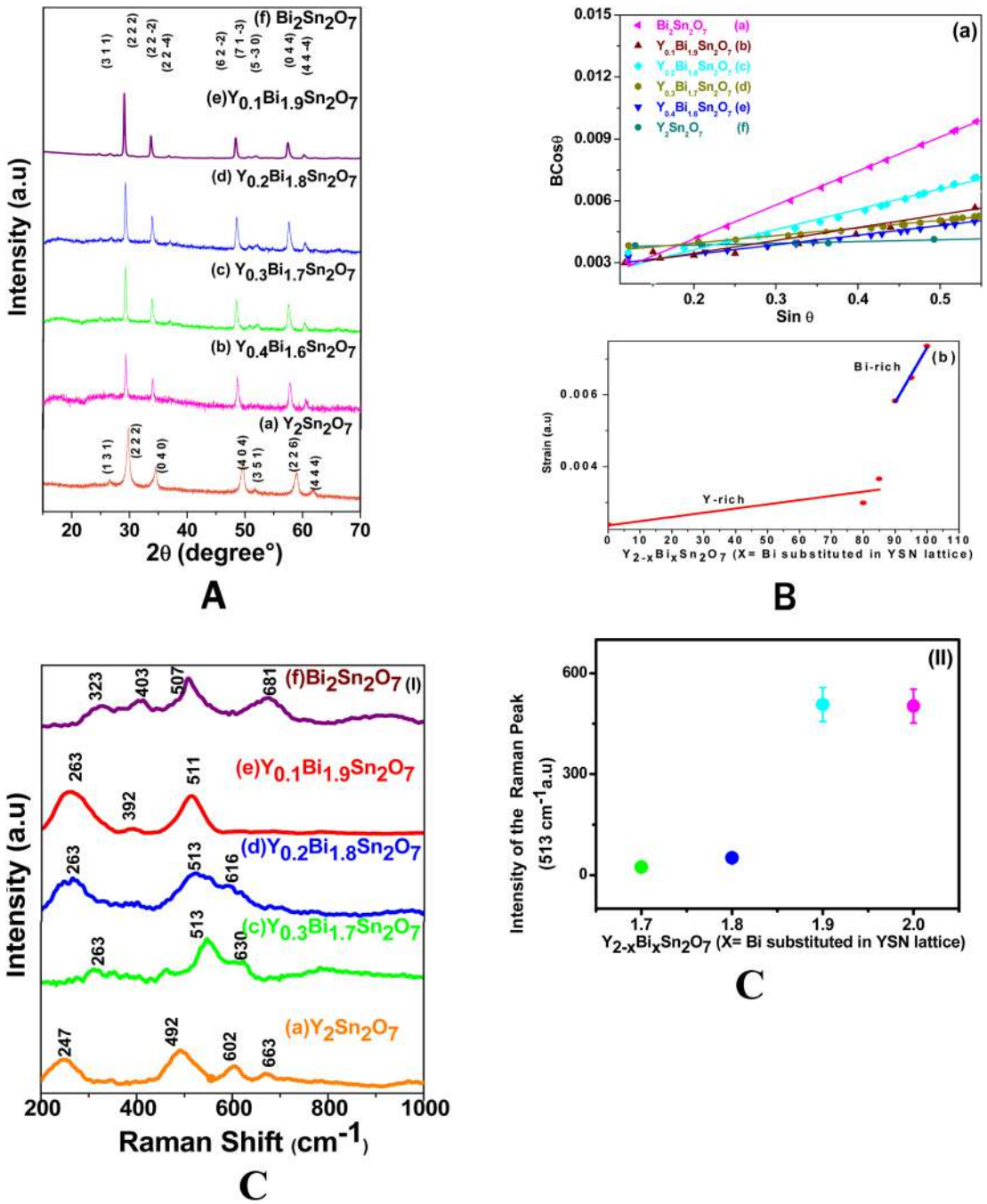

Fig. 1 (A) X-ray diffraction data for the different $Y_{2-x}Bi_xSn_2O_7$ catalysts: (a) YSN; (b) $Y_{0.4}Bi_{1.6}Sn_2O_7$; (c) $Y_{0.3}Bi_{1.7}Sn_2O_7$; (d) $Y_{0.2}Bi_{1.8}Sn_2O_7$; (e) $Y_{0.1}Bi_{1.9}Sn_2O_7$; (f) BSN. (B) (a) Calculation of strain over different catalysts and (b) change in strain as a function of Bi substitution. (C) (I) Raman spectra of different samples. (II) Plot of the intensity of the 513 cm^{-1} peak as function of Bi substitution in YSN.

where B = broadening (in radian) as calculated from Rietveld refinement, t = crystallite size and η = strain.

A thorough Rietveld analysis was performed for the Bi-substituted YSN systems and the cell parameters were derived from the Rietveld analysis and reflected in Table 1. The peak broadening for all the peaks was also calculated using the Rietveld analysis and used to find B [broadening (in radians), as in eqn (1)]. These results were utilised to construct the Williamson–Hall plot to calculate the strain, as portrayed in Fig. 1B. The plot of strain *versus* Bi-substitution is displayed in Fig. 1B(b), showing the effect of strain is quite high in the Bi-rich regions. The strain increased with an increase in Bi-substitution, which is evident in the above-mentioned figure.

3.2. Raman spectroscopy

A Raman investigation was performed on all the samples to understand the effect of asymmetry on the formed pyrochlores or pyrochlore-like structures. As understood earlier in the XRD

Table 1 Crystal lattice parameters, crystallite size, strain and BET surface area data

Sl no.	Samples	Lattice parameter[a] (Å)			Unit cell volume (Å^3)	Strain[b]	Crystallite size[c] (nm)	BET surface area[d] (m^2 g^{-1})
		a	*b*	*c*				
1	YSN	10.4008(3)	10.4008(3)	10.4008(3)	1125.13(1)	0.00238	24.7	9.8
2	$Y_{0.4}Bi_{1.6}Sn_2O_7$	12.9831(3)	7.5340(4)	15.0203(3)	1208.87(3)	0.00269	22.8	9.3
3	$Y_{0.3}Bi_{1.7}Sn_2O_7$	13.0900(3)	7.5284(3)	15.0649(3)	1207.61(4)	0.00366	22.4	9.6
4	$Y_{0.2}Bi_{1.8}Sn_2O_7$	13.06922(3)	7.5069(3)	15.1214(3)	1214.55(7)	0.00583	22.3	9.5
5	$Y_{0.1}Bi_{1.9}Sn_2O_7$	13.0576(4)	7.5305(3)	14.9999(3)	1204.52(2)	0.00648	22.3	9.1
6	BSN	13.03053(3)	7.54179(4)	15.0015(4)	1202.16(1)	0.00736	22.2	9.9

[a] Lattice parameter and unit cell volume obtained from the Rietveld study. [b] The strain was calculated from Rietveld refinement (calculated using the Williamson–Hall equation). [c] Crystallite size calculated using the Williamson–Hall equation (from the XRD data with specific 2θ and the required FWHM). [d] Calculated from N_2-adsorption studies (BET).

segment, YSN is a cubic pyrochlore with 13 vibrational modes, as presented in the irreducible representation in eqn (2). Here, in the case of YSN, there are six Raman-active modes and seven IR-active modes in vibration spectroscopy (eqn (2)).[41–43]

$$\Gamma = A_{1g} + E_g + 4T_{2g} + 7T_{1u} \quad (2)$$

The A-site and B-site (of $A_2B_2O_7$) cations do not contribute to the vibrations given that they are located on the inversion centre and only vibrations of the oxide ions are allowed.[37,44,45] A regular pyrochlore structure manifests six Raman-active modes designated as $A_{1g} + E_g + 4T_{2g}$. The Raman peak at ~533 cm^{-1} is assigned to A_{1g} (corresponding to O–B–O bending vibrations).

However, the BSN crystal adopts a tetragonal crystal structure, specifically classified in the *Pc* (C_{2s})[33] space group. This particular structure compels all 176 unique atomic positions with irreducible representations of eqn (3).

$$\Gamma_R = 526A' + 527A'' \quad (3)$$

In the case of a low symmetric material, all phonons characteristic of the ideal pyrochlore structure are permitted. The T_{1u} modes associated with the ideal pyrochlore structure correspond to O–Bi–O bending, O–Bi–O bending, and Bi–SnO_6 stretching vibrations. The bands observed at 507 cm^{-1} (A_{1g}) are typically attributed to O–Sn–O bending and Sn–O stretching.[46–48]

This activation stems from the interplay between the irreducible representations of both point groups. The Raman spectra acquired for BSN (Fig. 1C(I)(f)) exhibit bands at approximately 323, 407, and 681 cm^{-1}, together with an additional band at roughly 507 cm^{-1}.[49–51] The bands observed in the range of 200–380 cm^{-1} are attributed to the O–Sn–O bending and Bi–O stretching vibrations (T_{2g}). The two bands located at 407 cm^{-1} and 507 cm^{-1} result from the combination of (A_{1g}) and (T_{2g}/T_{1u}) modes. Here, the band at 407 cm^{-1} is ascribed to

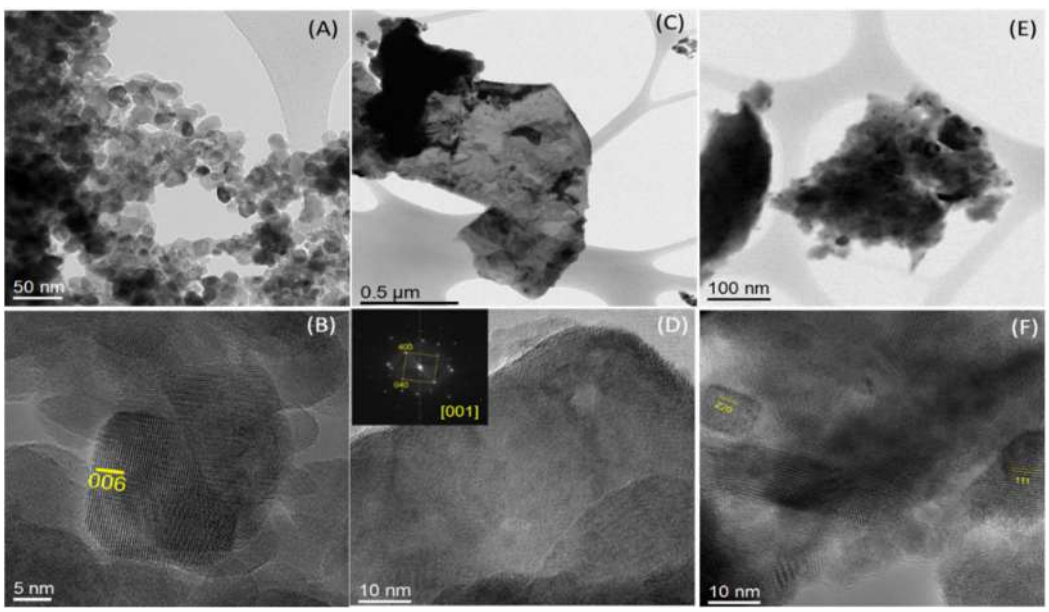

Fig. 2 TEM and HR-TEM images of BSN (A and B); $Y_{0.4}Bi_{1.6}Sn_2O_7$ (C and D), and YSN (E and F), and the inset in (D) shows the fast Fourier transform (FFT) of the HRTEM image, showing the [001] grain facet.

O-motion within the SnO_6 polyhedra (T_{2g}), while the band at 507 cm^{-1} is attributed to Bi–O′ stretching (T_{1u}).[45–47]

Shifting focus to the transition from YSN to BSN upon Bi-substitution in the YSN lattice, the resulting Raman peaks were predominantly observed at 263 cm^{-1}, 515 cm^{-1}, and 630 cm^{-1} [as depicted in Fig. 1C(I)(c)–(e)], respectively. Notably, the $Y_{0.1}Bi_{1.9}Sn_2O_7$ sample exhibited an additional peak at 392 cm^{-1}. The peak at 263 cm^{-1} is assigned to O–Sn–O bending. The prominent band observed at 515 cm^{-1} can primarily be attributed to the Bi–O stretching vibration. This band exhibits a pronounced intensification with increasing Bi content, suggesting a progressive enhancement in Bi–O interactions.[46,52] Conversely, the band at 630 cm^{-1} is predominantly ascribed to overtone and combination bands, reflecting a lesser degree of structural influence. Notably, the spectrum of $Y_{0.1}Bi_{1.9}Sn_2O_7$ reveals an additional peak at 392 cm^{-1}, which aligns with literature reports attributing this mode to Bi–O stretching vibrations.[53] Consequently, in Bi-substituted and BSN systems, the band centred at around 510 cm^{-1} requires particular attention. This band, present in all Bi-containing catalysts including BSN, predominantly represents the Bi–O stretching mode (T_{1u}). Therefore, the intensity of this band will serve as a qualitative marker for the phononic contribution, and as illustrated in Fig. 1C(II), it proportionally increased with an increase in the Bi content in the YSN system.[49] Given the lower structural symmetry inherent to Bi-substituted systems, as shown by the presence of a significant quantity of BiO_6 (as will be subsequently established through EXAFS data), their structural characteristics bear a closer resemblance to BSN compared to the symmetric pyrochlore structure of YSN. This is further shown in Fig. 1C(II), which clearly depicts the corresponding enhancement in the phononic contribution with an increase in Bi content. Also, according to the XRD studies, the lattice strain increased with Bi-substitution in the YSN lattice. The higher the strain, the more phononic coupling part in the lattice. This is also a definite indicator of an increment in the higher phononic coupling for the higher Bi-substituted materials. This observation will have very significant effect on materials possessing indirect band gaps, where a higher phononic part will lead to a higher lifetime of holes/electrons.

3.3. Morphological studies (TEM, HR-TEM, elemental mapping, FE-SEM and SAED studies)

The HRTEM image (Fig. 2A) of the BSN catalyst shows different planes, with the calculated *d*-spacing of 3.35 nm and the particle size of ∼5–8 nm. The SAED figure was indexed to different planes, the calculation of which is reported in the ESI (Table S.3).† The FE-SEM images together with the respective EDS patterns and elemental mapping of BSN, YSN and $Y_{0.4}Bi_{1.6}Sn_2O_7$ are shown in Fig. 3.

3.4. Zeta potential analysis

The zeta potential serves as a crucial parameter for determining the effective surface potential established by the formed electrical double layer at the interface between the Bi-substituted YSN photocatalysts and the surrounding aqueous environment. Considering the photocatalytic degradation of *p*-CP in water as an essential solid–liquid interphase reaction, any alterations in the surface charge of the photocatalyst will exert a considerable influence on both the adsorption process and the subsequent evolution of various intermediate species during photo-oxidation. Fig. 4A depicts the zeta potential of the compounds in the $Y_{2-x}Bi_xSn_2O_7$ series as a function of pH conditions. As readily observed in this figure, all the photocatalysts exhibit a negative surface charge. When analysing the impact of Bi-substitution on YSN at a slightly acidic pH of 6 (which closely mimics the conditions of the aqueous *p*-CP solution), BSN demonstrated the most negative surface charge, while YSN possessed the least negative surface charge. Furthermore, the surface charge progressively became more negative with an increase in Bi-substitution (Fig. 4A(b)). However, under more acidic conditions (pH 4), while the general trend regarding the surface charge of the $Y_{2-x}Bi_xSn_2O_7$ photocatalysts remained consistent, their overall surface charge became significantly less negative compared to that observed at pH 6 (Fig. 4A(a)). Even at a near-neutral pH of 8, the observed trend persisted, with BSN exhibiting the most negative surface charge across the entire pH range (Fig. 4A(c)).

Scheme 3 inherently depicts surfaces acquiring a negative charge. In the case of the YSN system, this translates to a greater abundance of H^+ ions adsorbed on its surface at lower pH values. This phenomenon leads to a reduction in its overall surface charge. Conversely, under higher pH conditions characterized by an abundance of OH^- ions, the hydroxyl groups abstract surface H^+ ions, resulting in an augmentation of the surface charge (Fig. 4B(e)).This trend can be explained with the help of the representative schematics shown in Schemes 3–5 for the required surfaces.

The BSN system exhibits distinct behaviour. Here, its surface possesses a negative surface charge. This surface charge becomes less negative to a certain extent at lower pH due to the presence of a high H^+ concentration, which competes for the surface sites. However, at a higher pH, the surface charge should decrease due to the prevalent OH^- ions, and thus competition arises for counter ions/H^+ (present in the H_2O medium) between OH^- and the BSN surface. Given that BSN possesses a greater surface negative charge (compared to OH^-), it preferentially acquires H^+/counter ions, leading to a significant increment in surface charge (Fig. 4B(a)). The surface negative charge of these materials can also be due to the presence of O-vacancies, which is verified later by XPS and EPR studies.

3.5. Diffused reflectance spectroscopy (DRS) studies

The DRS study for the samples is portrayed in Fig. 5. A distinct alteration in band gap was observed upon structural transformation and elemental substitution. This figure depicts the DR-UV-visible spectra acquired for the pristine YSN samples and those substituted with Bi^{2+} ions. Curves 'a' to 'e' exhibit a pronounced red shift relative to the spectrum of the unsubstituted YSN (curve 'f'). This red shift increased progressively with an increase in Bi concentration within the YSN lattice.

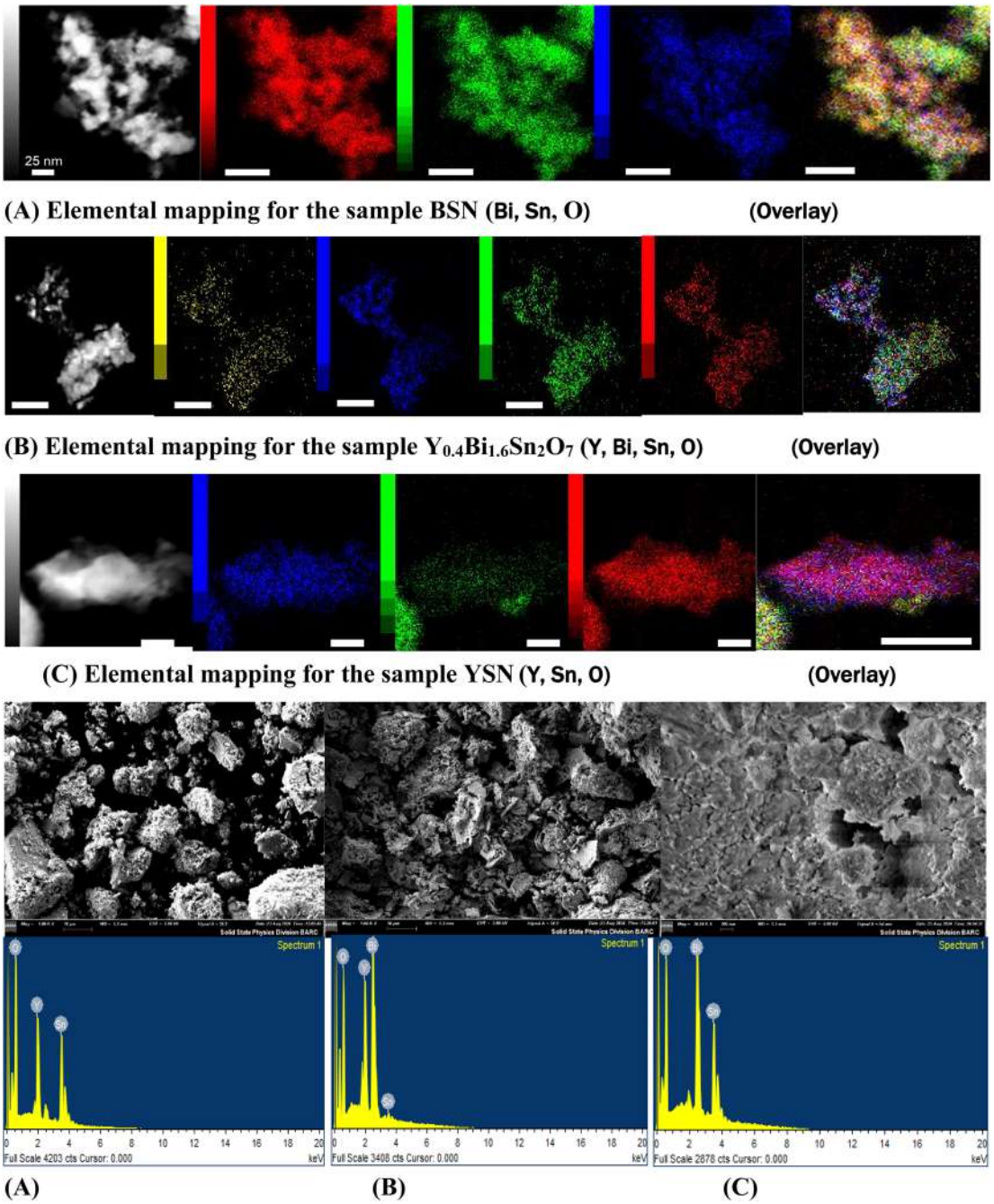

Fig. 3 First three horizontal panels show elemental mapping; the last two panels show FESEM images and EDS patterns for the different catalysts: (A) BSN, (B) $Y_{0.4}Bi_{1.6}Sn_2O_7$ and (C) YSN (EDS table in ESI†).

Notably, all the catalysts, with the exception of the parent YSN, exhibit a band gap situated within the visible region of the electromagnetic spectrum. The optical band gap energy (E_g) was quantitatively estimated by plotting the Kubelka–Munk function $F(R)$, as detailed in eqn (4) below.

$$F(R) = A(h\nu - E_g)^{m/2} \quad (4)$$

where $h\nu$ = photon energy and m is a constant that depends on the nature of the optical transition. The Kubelka–Munk plots for these materials are presented in Fig. 5. The band gap values varied from ~3.73 eV to 2.17 eV with an increase in Bi-substitution in YSN. Given that all samples were subjected to pre-treatment at 750 °C prior to the band gap measurements, the influence of particle size on their band gap can be effectively ignored.

The valence band of YSN lies in close proximity to the Fermi level. Consistent with the literature,[50] it can be inferred that the indirect band gap of the YSN system is comprised of a valence band (VB) formed primarily by O 2p orbitals with a minor

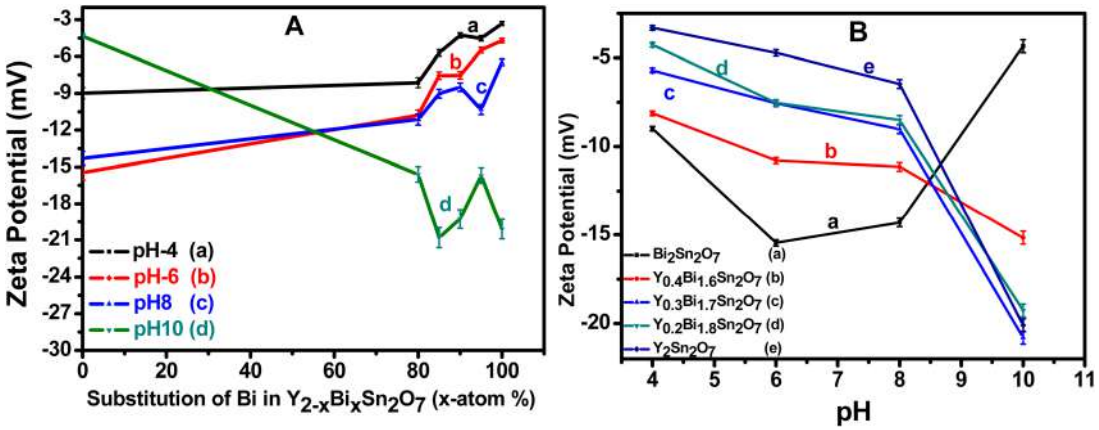

Fig. 4 (A) Plot of zeta potential at different pH values: (a) pH 4; (b) pH 6; (c) pH 8 and (d) pH 10 as a function of Bi-substitution in the YSN lattice. The bar at each point represents the error bar from the average of three sets of data taken for the same pH. (B) Plot of zeta potential at different pH values for the following samples: (a) BSN; (b) $Y_{0.4}Bi_{1.6}Sn_2O_7$; (c) $Y_{0.3}Bi_{1.7}Sn_2O_7$; (d) $Y_{0.2}Bi_{1.8}Sn_2O_7$; (e) YSN.

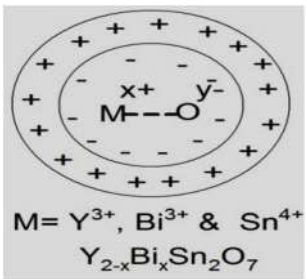

Scheme 3 Formation of the Helmholtz double layer for effective surface charge definition.

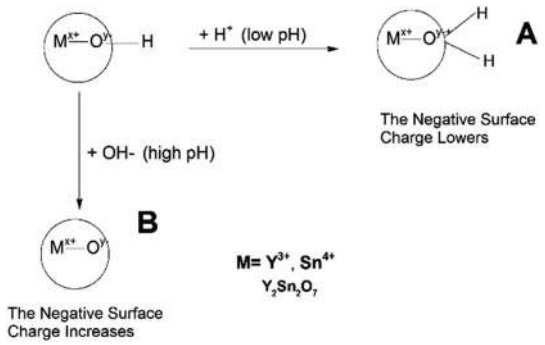

Scheme 4 Alteration in surface charge of YSN as a function pH.

contribution from the Sn 5s and 5p orbitals. The conduction band (CB) consists mainly of Sn 4d orbitals in conjunction with Y 5d orbitals in a lower portion. The occupied O 2p electron density migrates to the conduction band of the Sn-cations when they deviate from their equilibrium positions.

BSN is classified as an indirect band gap material exhibiting a band gap of 2.17 eV (Fig. 5f).[9] Based on its density of states,[9,54] its valence band (VB) is principally composed of O 2p and Bi 6s orbitals, hybridized with Sn 4d orbitals. Its conduction band (CB) is primarily composed of Bi 6p, Sn 5s, and partial admix of O 2p orbitals. The hybridized states of the VB and CB predominantly demonstrate the involvement of Sn 5s and Bi 6s orbitals, suggesting a high degree of mobility for the photo-induced electron density. Therefore, for all the samples in the $Y_{2-x}Bi_xSn_2O_7$ series, their VB will invariably possess contributions from Bi 6s and Sn 4d, alongside O 2p, Sn 5s, and 5p orbitals. All the other samples also exhibit indirect band gaps, and their photocatalytic properties will be predominantly governed by the occupancy of Bi 6s orbitals.

3.6. X-ray photoelectron spectroscopy (XPS)

XPS serves as a powerful tool for quantifying the binding energies of electrons associated with ions within a material. Fig. 6B depicts the binding energies corresponding to the O 1s peaks for all samples in the $Y_{2-x}Bi_xSn_2O_7$ series (where x is in the range of 0 to 1.6). The O 1s peaks of YSN appeared at 531.6 eV and 529.2 eV. The peak located at 531.6 eV exhibits a higher intensity compared to its counterpart at 529.2 eV. Furthermore, the observed peak position shifted with compositional variations, confirming their exclusive association with the pyrochlore structure. As previously established in the literature,[55–57] pyrochlores typically have two distinct oxygen environments, as reflected by the presence of two oxygen peaks in the XPS spectra.

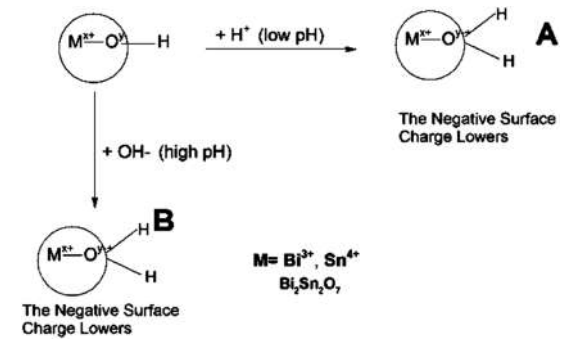

Scheme 5 Alteration in surface charge of BSN as a function pH.

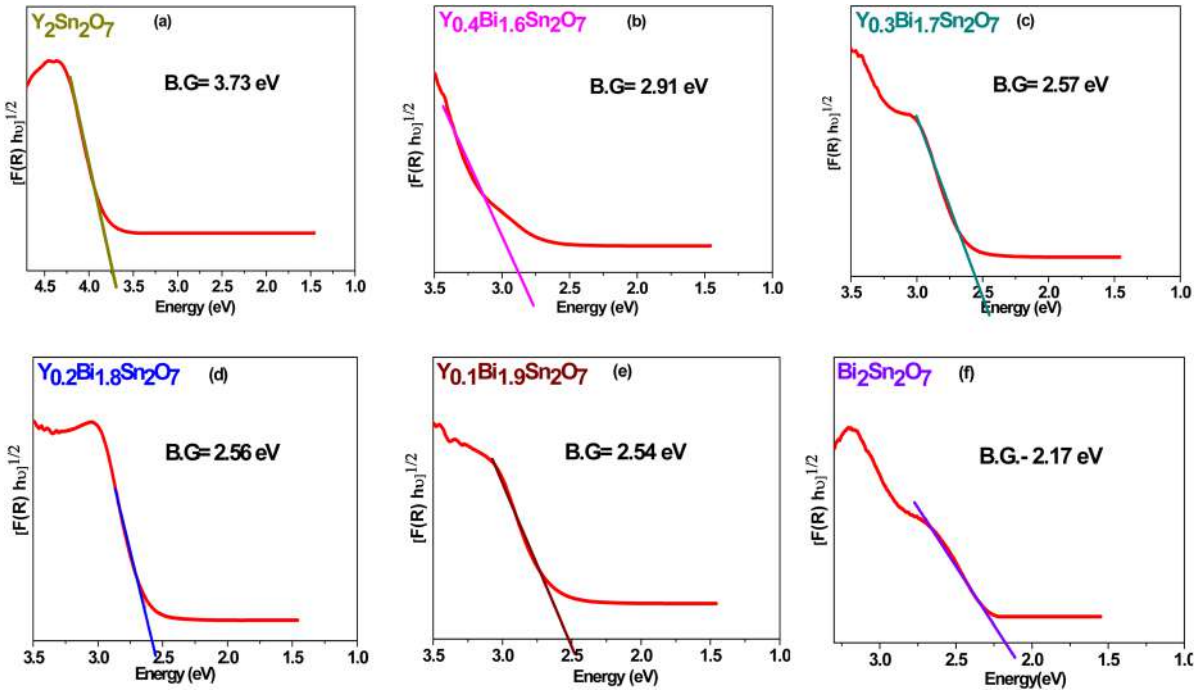

Fig. 5 Kubelka–Munk plots for the band gap of the different photocatalysts: (a) YSN; (b) $Y_{0.4}Bi_{1.6}Sn_2O_7$; (c) $Y_{0.3}Bi_{1.7}Sn_2O_7$; (d) $Y_{0.2}Bi_{1.8}Sn_2O_7$; (e) $Y_{0.1}Bi_{1.9}Sn_2O_7$; (f) BSN.

Earlier discussions highlighted that YSN possesses two types of oxygen atoms, six oxygen atoms (48f) surrounded by two Y^{3+} ions and two Sn^{4+} ions, and one oxygen atom (8b) surrounded solely by four Y^{3+} ions. The ionic character of the Y–O bond surpasses that of the Sn–O bond. Consequently, the 48f oxygen, surrounded by both Y^{3+} and Sn^{4+} ions, is expected to exhibit a higher binding energy than the 8b oxygen, which is exclusively surrounded by Y^{3+} ions. Based on this reasoning, it can be inferred that the peak at 531.6 eV corresponds to the 48f oxygen, while the peak at 529.2 eV can be assigned to the 8b oxygen.[52] In an ideal scenario, the intensity of the 48f oxygen peak should be significantly higher than that of the 8b oxygen peak. However, this is not observed in the present case, given that YSN is not a perfectly ordered pyrochlore. This structural imperfection contributes to the observed discrepancy in the intensity of the 48f oxygen peak, which is lower than expected. The inherent oxygen vacancy is associated with the 48f oxygen atom. As evident in Table 2, the percentage of 48f oxygen diminished progressively as a function of Bi-substitution within the YSN lattice. This observation implies a lower abundance of 48f oxygen in the samples with higher Bi-substitution levels. Subsequent XAS studies conclusively demonstrated that the coordination numbers around Y and Sn are 8 and 6, respectively, leading to the formation of cubic polyhedra surrounding Y and octahedra surrounding Sn. In an ordered pyrochlore structure, the coordination numbers of the 'A' and 'B' cations are eight and six, respectively, as previously illustrated. However, in the case of BSN, the data presented in Table 3 clearly indicates that the coordination number around Bi is 5, while that around Sn remains 6. This observation signifies a completely disordered pyrochlore structure. Consequently, the O 1s spectrum of BSN exhibits three peaks at 527.8 eV, 529.59 eV, and 531.58 eV, which do not directly correspond to the 48f and 8b peaks observed in YSN. This is further understood in the EPR section.

In the BSN crystal lattice, bismuth (Bi) exhibits a coordination number of five with respect to oxygen (O) atoms, while tin (Sn) maintains a coordination number of six. This translates to Bi existing primarily in the form of Bi polyhedra (BiO_5) and Sn existing primarily as Sn octahedra (SnO_6). As previously established, in YSN, the yttrium (Y) cations adopt a cubic polyhedral (YO_8) coordination environment, while Sn also remains coordinated by six oxygen atoms in an octahedral arrangement (SnO_6). The XPS peak at a binding energy of 527.8 eV is attributed to Bi^{3+} in the BiO_5 polyhedra, while the peak at 529.59 eV represents the O-atom associated with the Sn–O bond (SnO_6 octahedra). Finally, the peak at 531.58 eV corresponds to surface O-vacancy, as previously reported by Xu *et al.*[58,59] The extent of O-vacancy is less in the case of BSN compared to that of YSN. This unique environment creates two distinct electronic configurations for Bi, *i.e.*, one associated with the Bi–O bond within the BiO_5 polyhedra and another associated with the Bi–O bond, where the oxygen atom is simultaneously coordinated to a Y cation (Bi–O–Y). Thus, Bi experiences two distinct electron density distributions, leading to a difference in binding energies. Fig. 6A depicts the deconvoluted XPS spectra of Bi 4f electrons with spin–orbit splitting for the $Y_{0.4}Bi_{1.6}Sn_2O_7$ sample with binding energies of 156.7 eV and 158.8 eV (Bi $4f_{7/2}$ level). The lower energy peak (156.7 eV) can be attributed to Bi-interaction with the oxygen atom bound to Y cations (Bi–O–Y).

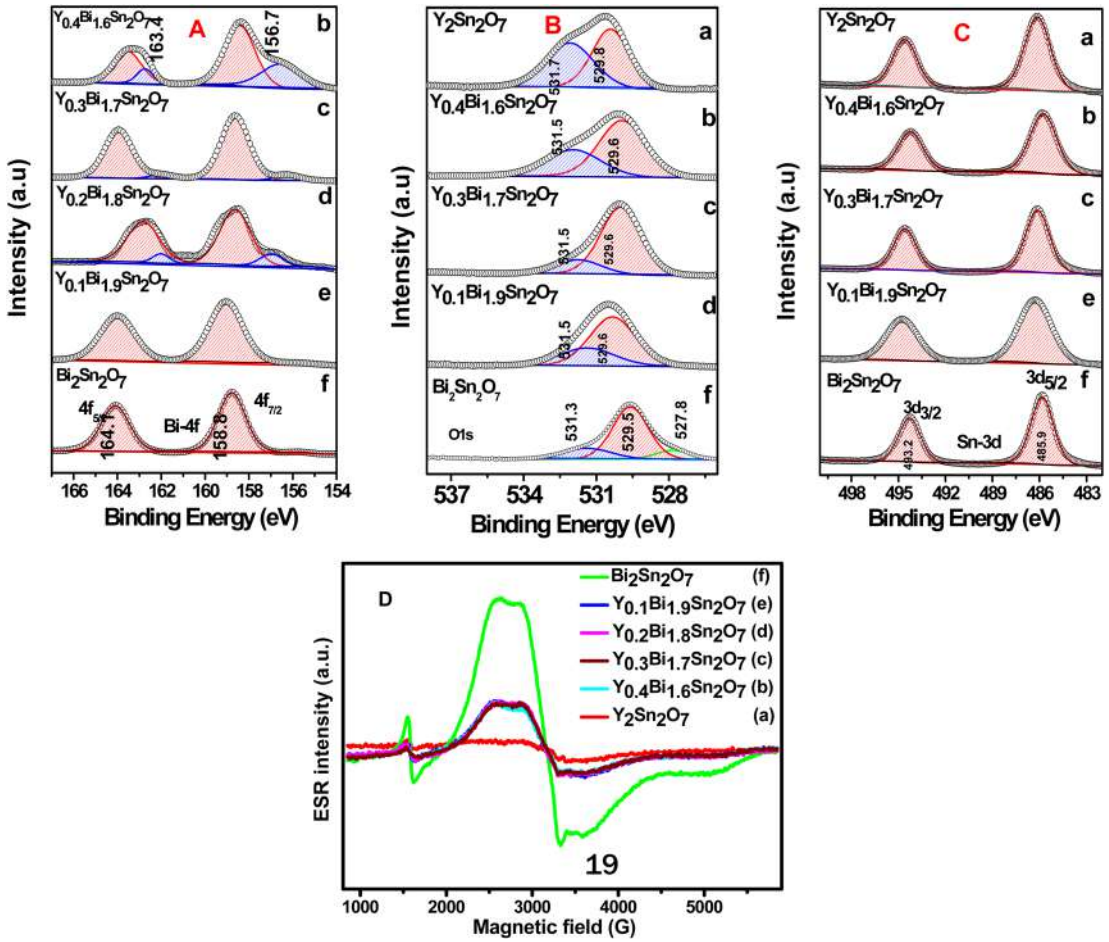

Fig. 6 (A) XPS data for deconvoluted Bi 4f with LS splitting of $4f_{7/2}$ and $4f_{5/2}$, (B) deconvoluted O 1s, (C) deconvoluted Sn 3d with LS splitting of $4d_{5/2}$ and $4d_{3/2}$ for different samples. (D) EPR for the samples for different samples: (a) YSN; (b) $Y_{0.4}Bi_{1.6}Sn_2O_7$; (c) $Y_{0.3}Bi_{1.7}Sn_2O_7$; (d) $Y_{0.2}Bi_{1.8}Sn_2O_7$; (e) $Y_{0.1}Bi_{1.9}Sn_2O_7$; (f) BSN.

Table 2 Table showing the percentage of different types of O 1s species present in the different pyrochlores

Sl no.	Sample	Peak position (eV)	FWHM (eV)	Percentage (%)
1	YSN	529.78	1.94	51.06
		531.59	2.49	48.94
2	$Y_{0.4}Bi_{1.6}Sn_2O_7$	529.78	1.96	64.4
		531.20	2.52	35.6
3	$Y_{0.3}Bi_{1.7}Sn_2O_7$	529.98	2.2	69.6
		531.75	2.69	30.4
4	$Y_{0.1}Bi_{1.9}Sn_2O_7$	529.4	1.96	81
		531.4	2.21	19
5	BSN	527.8	1.7	12
		529.54	1.73	68.19
		531.54	2.41	19.91

Conversely, the higher binding energy corresponds to Bi within the BiO_5 polyhedra. As the Bi-substitution increases, a greater number of Bi–O bonds is formed within the BiO_5 polyhedra, leading to an associated decrease in the population of Bi–O–Y interactions.

Ultimately, with complete Bi-substitution (resulting in the formation of BSN), the Bi–O–Y interactions become negligible, as confirmed by the structural studies of the Bi-substituted YSN materials. Examination of the Sn 3d XPS spectrum (Fig. 6(c)) reveals two prominent peaks at binding energies of 486.1 eV and 494.5 eV, corresponding to the Sn $3d_{5/2}$ and Sn $3d_{3/2}$ levels, respectively. The observed spin–orbit splitting of 8.4 eV is consistent with the characteristic signature of Sn^{4+} ions within a pyrochlore structure.[60] Notably, the X-ray absorption spectroscopy (XAS) studies (discussed subsequently) confirm the transformation of Bi-coordination from YO_8 in YSN to BiO_5 polyhedra upon Bi substitution. However, this alteration in the Bi environment did not significantly impact the electronic configuration surrounding the Sn^{4+} ions. This can be attributed to the inherent preference of Sn^{4+} for a six-fold coordination geometry, which was maintained throughout the series.

The Y 3p XPS spectrum exhibits two peaks at 300.3 eV and 312.1 eV, which can be assigned to the Y $3p_{3/2}$ and Y $3p_{1/2}$ levels, respectively. The energy separation (ΔE) of 11.8 eV is consistent with the established signature for Y^{3+} cations.[61] Interestingly, the binding energy of Y^{3+} remained remarkably stable despite the variations in the Bi^{3+} concentration. Although Bi-

Table 3 Bond length, coordination number and disorder factors obtained using EXAFS fitting measured at Sn K-edge and Bi L-edge

Sn K edge							
Path	Parameter	YSN	$Y_{0.4}Bi_{1.6}Sn_2O_7$	$Y_{0.3}Bi_{1.7}Sn_2O_7$	$Y_{0.2}Bi_{1.8}Sn_2O_7$	$Y_{0.1}Bi_{1.9}Sn_2O_7$	BSN
$Sn–O_2$	R (Å) (2.05)	2.05 ± 0.01	2.05 ± 0.01	2.05 ± 0.01	2.05 ± 0.01	2.05 ± 0.01	2.05 ± 0.01
	N (6)	6 ± 0.14	6 ± 0.21	6 ± 0.21	6 ± 0.28	6 ± 0.21	6 ± 0.21
	σ^2	0.0046 ± 0.0005	0.0033 ± 0.001	0.0011 ± 0.0005	0.0012 ± 0.0006	0.0011 ± 0.0006	0.0023 ± 0.0006
Sn–Y or Sn–Bi	R (Å) (3.7)	3.55 ± 0.05	3.54 ± 0.04	3.50 ± 0.06	3.46 ± 0.04	3.49 ± 0.05	3.59 ± 0.16
	N (6)	6 ± 0.14	6 ± 0.21	6 ± 0.21	6 ± 0.28	6 ± 0.21	6 ± 0.21
	σ^2	0.018 ± 0.006	0.015 ± 0.005	0.018 ± 0.009	0.014 ± 0.005	0.015 ± 0.008	0.03 ± 0.01
Sn–Sn	R (Å) (3.7)	3.79 ± 0.06	3.79 ± 0.03	3.81 ± 0.01	3.82 ± 0.01	3.81 ± 0.02	3.71 ± 0.02
	N (6)	6 ± 0.14	6 ± 0.21	6 ± 0.21	6 ± 0.28	6 ± 0.21	6 ± 0.21
	σ^2	0.027 ± 0.01	0.015 ± 0.005	0.0055 ± 0.002	0.0049 ± 0.002	0.0055 ± 0.002	0.0094 ± 0.002
R-factor		0.008	0.01	0.02	0.02	0.02	0.02
Bi-L_3 edge							
Path	Parameter	$Y_{0.4}Bi_{1.6}Sn_2O_7$	$Y_{0.3}Bi_{1.7}Sn_2O_7$	$Y_{0.2}Bi_{1.8}Sn_2O_7$	$Y_{0.1}Bi_{1.9}Sn_2O_7$	BSN	
$Bi–O_1$	R (Å) (2.27)	2.15 ± 0.01	2.18 ± 0.01	2.19 ± 0.01	2.19 ± 0.01	2.19 ± 0.01	
	N (2)	2 ± 0.04	2 ± 0.04	2 ± 0.04	2 ± 0.02	2 ± 0.02	
	σ^2	0.0047 ± 0.0004	0.0041 ± 0.0007	0.0033 ± 0.00067	0.0037 ± 0.0004	0.0032 ± 0.0004	
$Bi–O_2$	R (Å) (2.42)	2.36 ± 0.02	2.26 ± 0.01	2.22 ± 0.01	2.29 ± 0.01	2.26 ± 0.01	
	N (3)	3 ± 0.06	3 ± 0.06	3 ± 0.06	3 ± 0.03	3 ± 0.03	
	σ^2	0.03 ± 0.003	0.008 ± 0.0007	0.0193 ± 0.0015	0.019 ± 0.009	0.025 ± 0.00113	
Bi–Sn	R (Å) (3.56)	3.60 ± 0.02	3.61 ± 0.01	3.60 ± 0.01	3.67 ± 0.01	3.49 ± 0.01	
	N (4)	4 ± 0.08	4 ± 0.08	4 ± 0.08	4 ± 0.04	4 ± 0.04	
	σ^2	0.016 ± 0.0026	0.0098 ± 0.0009	0.011 ± 0.001	0.026 ± 0.0029	0.015 ± 0.0008	
Bi–Bi	R (Å) (3.90)	4.07 ± 0.06	3.79 ± 0.01	3.76 ± 0.02	3.77 ± 0.01	3.75 ± 0.01	
	N (6)	6 ± 0.12	6 ± 0.12	6 ± 0.12	6 ± 0.06	6 ± 0.06	
	σ^2	0.03 ± 0.008	0.01 ± 0.001	0.021 ± 0.003	0.019 ± 0.0018	0.0077 ± 0.0005	

substitution introduced BiO_5 polyhedra, subsequent XANES studies (discussed later) demonstrated that the Y-cations retained their distorted cubic coordination environment, forming YO_8 even in the substituted systems. Consequently, the electronic environment surrounding Y^{3+} remained unaltered, as will be further corroborated by the forthcoming XANES analysis.

3.7. Electron paramagnetic resonance (EPR) studies

Fig. 6D shows two electrons paramagnetic resonance (EPR) signals. At around 2800 G, a broad EPR signal (with $g = 1.98$) appeared and a sharp signal at 1543 G (corresponding to $g = 4.02$). The EPR signal of YSN is very weak and that of BSN is very strong. The EPR signal increased as a function of Bi in the lattice. Bi was shown to be EPR active for the Bi^{5+} system in the $NaBiO_3$ and $BaBiO_{3-}\delta$ systems studied by Kharton *et al.*[62] However, no EPR signal appeared for the α-Bi_2O_3 system, where Bi is present as Bi^{3+}. Goovaerts *et al.*[63] showed the respective EPR signal for the highly paramagnetic Bi_M^{4+} centre at 100 K identified with the isotropic non-substituted $Bi_{12}GeO_{20}$ and $Bi_{12}SiO_{20}$ systems upon blue light illumination, which majorly influenced the EPR intensity.[63] Given that Bi^{3+} is diamagnetic, it is not EPR active. The previous XPS experiments confirmed that Bi is only present in the Bi^{3+} state and there is no Bi^{4+} or Bi^{5+} states. Also, given that Sn^{4+} is diamagnetic in nature, the EPR signal of these materials must be a result of the O-vacancies, as obtained previously in the literature.[64] The formation of oxygen vacancies was indeed confirmed by the EPR measurements. The BSN system showed a very strong EPR signal at $g = 1.93$, which is consistent with the capture of electrons by oxygen vacancies in SnO_2.[46,47] The presence of oxygen vacancies was confirmed through EPR spectroscopy by the characteristic signal at the magnetic field of 3445 G, which is ascribed to the unpaired electrons associated with oxygen vacancies. This signal corresponds to the paramagnetic centres created by the absence of oxygen atoms in the lattice, which disrupts the electronic structure and results in a detectable EPR response at room temperature. The EPR signal obtained at $g = 1.98$ is quite broad in nature, which is mostly due to the anisotropic effect in the solid crystalline BSN. Similar results were obtained for the other Bi-substituted YSN catalysts. Here, with an increase in Bi-substitution, there was increase in O-vacancies, where the O-vacancies were the maximum for BSN. The XPS data also showed the formation of O-vacancies, which was again confirmed by the EPR experiments. However, as shown by EPR for the bulk effect and XPS for the surface effect, YSN contained more surface O-vacancies compared to that in BSN (Table 2), and according to EPR, the total bulk O-vacancies is greater in BSN compared to YSN, which increased as a function of Bi in the lattice.

3.8. X-ray absorption spectroscopy (XAS-EXAFS and XANES) studies

The experimental $\chi(R)$ *versus* R plots of the Bi-substituted YSN samples at the Y K edge, Sn K edge and Bi L edge were

simultaneously fitted from 1 to 4 Å assuming a pyrochlore structure with Bi-substitution at the Y site, as shown in Fig. 7. The EXAFS peaks observed at 1.5 Å and 3.5 Å correspond primarily to contributions from the Sn–O_1 and Sn–Sn_1 coordination shells, respectively. As can be observed in Table 3, the Sn–Y bond distance decreased and the Sn–Sn bond distance increased as the Bi concentration increased in the samples.

The EXAFS fitting results are tabulated in Tables 3 and 4. Notably, O-1 represents the oxygen atom occupying the 8b position, while O-2 represents the oxygen atom occupying the 48f position within the pyrochlore structure (as depicted for the fitting of the Bi-L edge and Y-K edge). In contrast, Table 2 only considers a single type of oxygen coordinated with Sn. During the fitting process, the coordination numbers for oxygen paths were varied, while the coordination numbers of all other paths were held constant to minimize the number of independent fitting parameters. Tables 3 and 4 present the impact of altering the coordination numbers for Y and Bi, while Table 3 focuses on the coordination number for Sn. Analysis of the Sn K-edge revealed a near-constant coordination number (C.N.) for Sn of approximately 6 ± 0.14 to ±0.28 across the Bi-substitution range. However, a significant alteration in the Sn–Bi distance compared to the Sn–Y distance was observed. Table 3 clearly demonstrates that the coordination number of Bi (O1–2) exhibited a minimal variation from $Y_{0.4}Bi_{1.6}Sn_2O_7$ to BSN, and the second coordination number (O2–3) remained nearly constant as a function of Bi substitution, collectively yielding an overall coordination number of 5.0 for Bi in all the compositions from BSN to $Y_{0.4}$ $Bi_{1.6}Sn_2O_7$. The EXAFS analysis for BSN confirmed a coordination number of 5 for Bi and 6 for Sn, suggesting the predominance of corner sharing with minimal edge sharing. This configuration maximizes the formation of Bi polyhedra around the Sn octahedra, resulting in a highly intricate unit cell. Interestingly, in the Bi-substituted YSN series, Bi retained a coordination number of 5, while Y maintained a coordination number of 8. This distinct coordination environment led to the formation of separate Bi polyhedra and cubic polyhedra surrounding Y, contributing to a highly predominant asymmetric crystal lattice, as previously observed.

Table 4 Bond length, coordination number and disorder factors obtained using EXAFS fitting measured at the Y K-edge

Y K edge			
Path	Parameter	YSN	$Y_{1.6}Bi_{0.4}Sn_2O_7$
Y–O_1	R (Å) (2.25)	2.23 ± 0.01	2.24 ± 0.01
	N (2)	2 ± 0.06	2 ± 0.06
	σ^2	0.0033 ± 0.001	0.005 ± 0.001
Y–O_2	R (Å) (2.49)	2.38 ± 0.01	2.37 ± 0.01
	N (6)	6 ± 0.18	6 ± 0.18
	σ^2	0.011 ± 0.000	0.012 ± 0.0009
Y–Y	R (Å) (3.67)	3.64 ± 0.01	3.65 ± 0.01
	N (6)	6 ± 0.18	6 ± 0.18
	σ^2	0.0085 ± 0.00	0.0084 ± 0.0007
Y–Sn	R (Å) (3.67)	3.65 ± 0.01	3.64 ± 0.01
	N (6)	6 ± 0.18	6 ± 0.18
	σ^2	0.011 ± 0.001	0.012 ± 0.001
R-factor		0.01	0.016

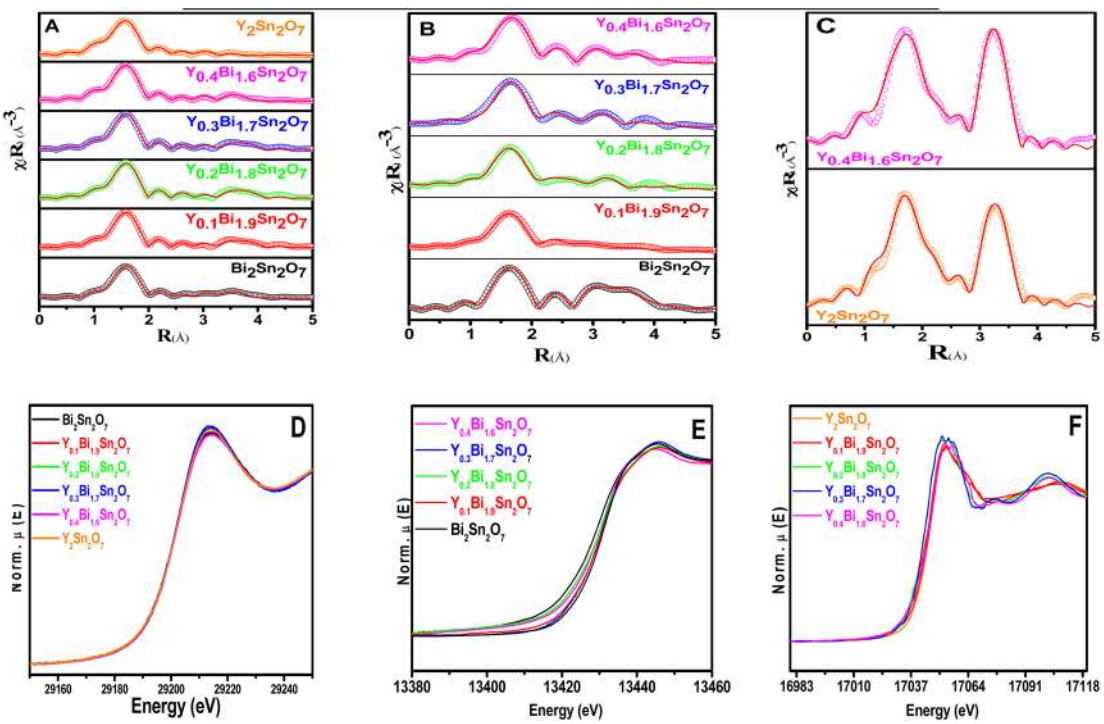

Fig. 7 Fourier transformed EXAFS spectra of $Y_xBi_{2-x}Sn_2O_7$ samples at (A) the Sn K-edge, (B) Bi L_3-edge and (C) Y L_3-edge (experimental data are represented by scatter points and theoretical fits are represented by solid lines). Normalized XANES spectra of $Y_{2-x}Bi_xSn_2O_7$ samples at (D) the Sn K-edge, (E) Bi L_3-edge and (F) Y K-edge.

The Bi–Sn distance exhibited a dependence on Bi-substitution, reaching a minimum value of 3.49 Å in BSN and increasing to 3.60 Å in $Y_{0.4}Bi_{1.6}Sn_2O_7$. This observation further corroborates the trends observed in the coordination numbers. Fig. 7A and B display the X-ray absorption near-edge structure (XANES) spectra of the Bi-substituted YSN samples at the Y K-edge and Bi L-edge, respectively. Consistent with the XPS findings, no significant variations in the oxidation state or effective positive charge surrounding Y were evident upon Bi-substitution, as observed in Fig. 7E. However, a clear alteration in the oxidation state around the Bi cations can be discerned in Fig. 7E. BSN exhibits a higher binding energy compared to $Y_{0.4}Bi_{1.6}Sn_2O_7$. Nonetheless, the transition from BSN to $Y_{0.4}Bi_{1.6}Sn_2O_7$ is not strictly monotonic.

This non-monotonic trend can be attributed to the following. Although the coordination number for Bi remained constant, the coordination number for Y was 8. Consequently, Bi atoms replacing Y occupied two distinct coordination environments, BiO_5 polyhedra and YO_8 polyhedra with a lower electropositive character due to the more polarizable Bi–O bond, as confirmed by subsequent XPS studies. Therefore, the BiO_5 units within the $Y_{0.4}Bi_{1.6}Sn_2O_7$ system attracted a greater electron density compared to the BiO_5 units in BSN, leading to a lower binding energy in the former. Conversely, the alteration in binding energy surrounding Y was negligible. As a result, Bi-substitution in YSN induced a slight decrease in the oxidation state compared to BSN. However, this observation is primarily qualitative and requires quantitative analysis using a Bi standard for definitive confirmation.

3.9. Photovoltaic switching and Mott–Schottky experiment

The selected BSN and YSN powders were transformed into thin films on appropriate substrates to facilitate photoelectrochemical measurements. The reusability of a photocatalyst is a critical parameter influencing its real-world applicability. Fig. 8 depicts the results of the "switch-on/off" experiments, which evaluated both the reusability of the photocatalysts and the photocurrent generated by them. As evident from Fig. 8D, the BSN photocatalyst exhibited the highest photocurrent among the compositions owing to its low band gap. Conversely, YSN (Fig. 8D) demonstrated the lowest photocurrent density under visible light irradiation. The photocurrents for these photocatalysts mostly increased with Bi-substitution in YSN. With an increase in Bi-substitution in YSN, the band gap of these materials decreased from 3.73 eV to 2.17 eV (Fig. 5).

A lower band gap has a positive effect on the photocurrent for a p-type semiconductor. The EPR and XPS studies confirmed the fact that the content of O-vacancies increased with Bi-substitution in these photocatalysts, which also led to the generation of a greater photocurrent. Generally, the overall photocurrent density (upon reaching saturation) increased with Bi-substitution in the YSN system (Fig. 8B–D). This observation aligns with the fundamental principles of photocatalysis, where a higher photocurrent signifies a greater abundance of holes in the valence band (VB) and electrons in the conduction band (CB). As the band gap decreased with an increase in the Bi substitution levels, the corresponding increase in photocurrent was observed. This suggests that BSN possesses superior photocatalytic properties among the compositions, primarily due to its narrower band gap. The consistent photovoltaic current together with the XRD data (Fig. S.29A†) and elemental XPS data for BSN before and after photocatalysis established the structural stability of these photocatalysts after photo-irradiation. Mott–Schottky (M–S) analysis is widely used to estimate the key operational parameters of semiconductor photo-electrodes, namely their flat-band potential, E_{fb}, and donor concentration, N (for an n-type semiconductor photoanode), or acceptor concentration, Na (for a p-type photocathode).

The Mott–Schottky relationship involves the apparent capacitance measurement as a function of potential under depletion conditions, as presented in eqn (5).

$$1/C^2 = \frac{2}{e\varepsilon\varepsilon_o N}\left(E - E_{fb} - kT/e\right) \quad (5)$$

The donor density can be calculated from the slope of the $1/C^2$ *vs.* E curve, and the flat-band potential can be determined by extrapolation to $1/C = 0$.

The model required for the calculation is based on two assumptions, as follows:

(a) Consideration of two capacitances: the capacitance related to the space charge region and the double layer capacitance. Given that these capacitances are in series, the total capacitance will be equal to the sum of their reciprocals. In this case, the space charge capacitance is much smaller compared to that of the double layer capacitance, and thus the contribution of the double layer capacitance to the total capacitance is almost negligible. Therefore, the capacitance value calculated from this model is assumed to be mainly value of the space charge capacitance.

(b) The equivalent circuit used in this model is a series combination of a resistor and a capacitance (the space charge capacitance). The capacitance is calculated from the imaginary component of the impedance [Im(Z)] using the following relationship (eqn (6)):

$$\mathrm{Im}(Z) = \frac{-1}{2\pi f_c} \quad (6)$$

The chosen model was demonstrated to be valid only under the condition that the frequency (f_c) is sufficiently high, exceeding the kilohertz (kHz) range. The slope of the $1/C^2$ *vs.* E plot in the Mott–Schottky analysis provides a means to identify the dominant carrier type in a semiconductor. A negative slope signifies a p-type semiconductor characterized by an abundance of hole acceptors (reduced donor density). The intercept of this plot at $C = 0$ corresponds to the flat-band potential (E_{fb}) of the material. As illustrated in Fig. 8, all the investigated photocatalysts exhibit negative slopes in their respective Mott–Schottky plots, classifying them as p-type semiconductors. However, these materials possess distinct Fermi energies due to their inherent compositional differences. Consequently, their

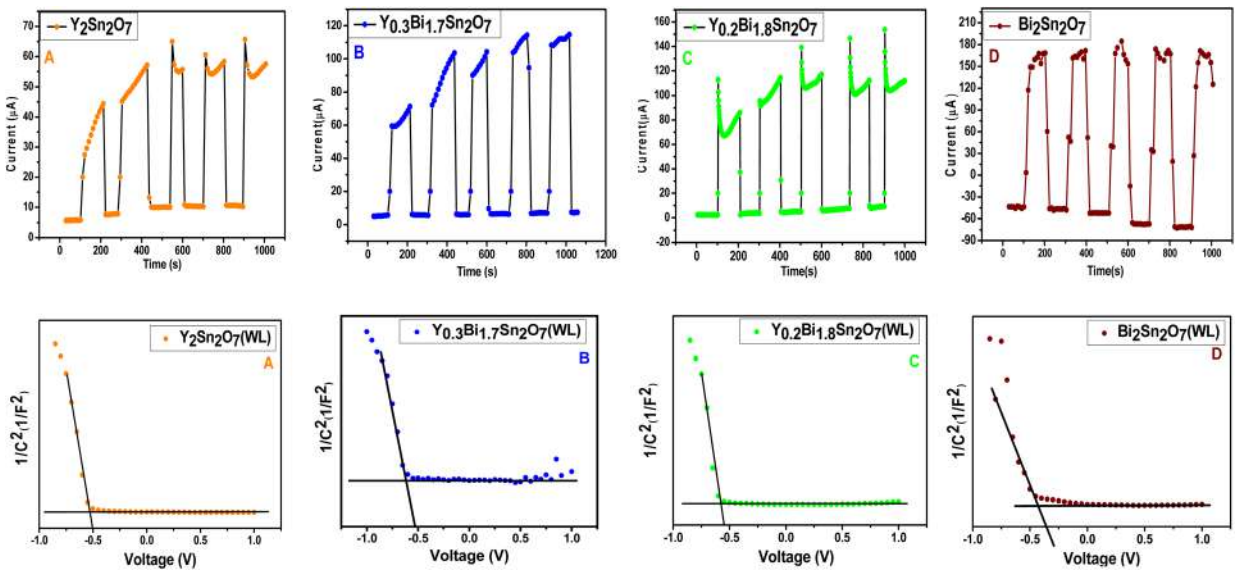

Fig. 8 (1) Top panel shows the switching experiment and (2) bottom panel shows the Mott–Schottky plots for the different photocatalysts with the KCl electrolyte: (A) YSN; (B) $Y_{0.2}Bi_{1.8}Sn_2O_7$; (C) $Y_{0.3}Bi_{1.7}Sn_2O_7$; (D) BSN.

dielectric constants ("ε" and "ε_0") also vary. This disparity precludes a direct comparison of donor density (N) solely based on the slope values. Nonetheless, the flat-band potential (E_{fb}) for each system was successfully determined from the intercept of the relevant equation. The valence band potential can be calculated from the E_{fb} calculation E_{KCl} (0.1 M) to SHE (pH 7) to SHE (pH 0) to vacuum, as reported by Xiao *et al.*[65] (eqn (7)–(9)).

(1) E_{KCl} (0.1 M) to SHE (pH 7) = 0.414 V.

(2) SHE (pH 7) to SHE (pH 0) = 0.2881 V.

(3) SHE (pH 0) to vacuum = 4.5 V (vacuum).

Thus,

$$\text{Valence band potential (VBp)} = E_{fb} - (0.414\ \text{V} + 0.2881\ \text{V} - 4.5\ \text{V}) = E_{fb} + 3.7979\ \text{V} \quad (7)$$

$$E_g = E_{VB} - E_{CB} \quad (8)$$

Thus,

$$E_{CB} = E_{VB} - E_g \quad (9)$$

The E_{VB} calculated from the Mott–Schottky plots is presented in Scheme 6.

The valence band potential for YSN is the lowest, which increased with Bi-substitution in the system, with BSN having the highest valence band potential of 3.44 eV. It can be noted that the valence band potential for BSN and all the other photocatalysts is quite low lying and lower as compared to the formation of $OH^{\bullet}$ from H_2O and OH^- from $OH^{\bullet}$.

3.10. Photocatalytic activity

The photocatalytic activity of the synthesized $Y_{2-x}Bi_xSn_2O_7$ (x = 0.0–2.0) samples was assessed through the degradation of *para*-chlorophenol (*p*-CP), a model organic pollutant, under visible light irradiation. The experimental details regarding the irradiation source were provided earlier. Notably, YSN, exhibiting a wider bandgap and absorbing only UV light, was also evaluated using a UV irradiation source for comparison. *Ex situ* FT-IR spectroscopy was employed as a complementary technique to elucidate the nature of the photocatalytic intermediates formed during the degradation of *p*-CP, thereby serving as a proof-of-concept for the reaction mechanism.

Fig. 9A depicts the variation in photocatalytic activity of the synthesized materials as a function of Bi-substitution. The detailed kinetic data for the individual photocatalysts are presented in the ESI (Fig. S.2–S.7).† It is crucial to note that the self-degradation of *p*-CP in the absence of a photocatalyst was negligible (Fig. S.1†). Consequently, the percentage of degradation products was calculated using eqn (10).

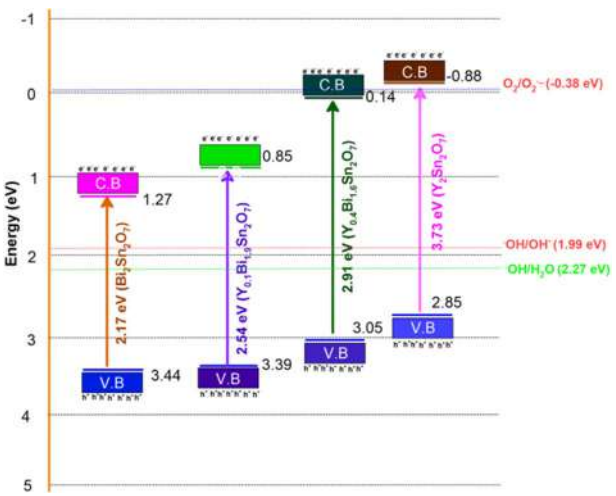

Scheme 6 Band potential analysis of the Bi-substituted YSN photocatalysts.

The product percentage (PC%) is

$$\mathrm{PC}(\%) = \frac{C_o - C_i}{C_o} \times 100 \quad (10)$$

where C_o = UV-vis intensity of *p*-CP without any catalyst and C_i = UV-vis intensity of *p*-CP without particular photocatalyst at time t_i.

To obtain a quantitative understanding, the catalytic activity of the different photocatalysts is shown in the inset of Fig. 9A as a plot of $t_{1/2}$ *vs.* Bi concentration in the YSN lattice. $t_{1/2}$ is defined as the half time taken to completely degrade *p*-CP, which can be taken as a measure of the photocatalytic activity of these photocatalysts. As observed in Fig. 9A, the $t_{1/2}$ of BSN is the lowest, which is about 15 min. Upon Bi-substitution, the photocatalytic activity ($t_{1/2}$) decreased, showing better activity under visible irradiation.

Conversely, the absence of *p*-CP self-degradation during the experiment confirmed its stability under ultraviolet (UV) irradiation from a lamp. The enhanced visible-light photocatalytic activity for *p*-CP degradation is attributed to the modulation of the electronic band structure of the pyrochlores induced by varying degrees of Bi-substitution. Notably, BSN exhibited the highest activity (100% degradation within 60 min). In comparison, the synthesized catalysts, YSN, $Y_{0.4}Bi_{1.6}Sn_2O_7$, $Y_{0.3}Bi_{1.7}Sn_2O_7$, $Y_{0.2}Bi_{1.8}Sn_2O_7$, and $Y_{0.1}Bi_{1.9}Sn_2O_7$, displayed degradation efficiencies of 80% (240 min), 90% (150 min), 93% (150 min), 98% (120 min), and 100% (90 min), respectively.

The apparent quantum efficiency (AQE) of the photocatalysts, as detailed in the ESI,† demonstrates a clear increase with Bi substitution. BSN exhibited the highest AQE of 0.45%, while YSN displayed the lowest (0.093%). This trend suggests a systematic enhancement in AQE with an increase in Bi-concentration in YSN. The AQE values for all the photocatalysts are provided in Table S.2 (ESI).† Fig. 9C depicts the photo-degradation of *p*-CP under UV irradiation. Ideally, the YSN catalysts, possessing a band gap of 3.7 eV (UV region), would be expected to outperform the BSN catalysts with a narrower band gap of 2.5 eV (visible region). However, Fig. 9C contradicts this expectation, where the BSN catalysts demonstrate a superior performance under UV light. This

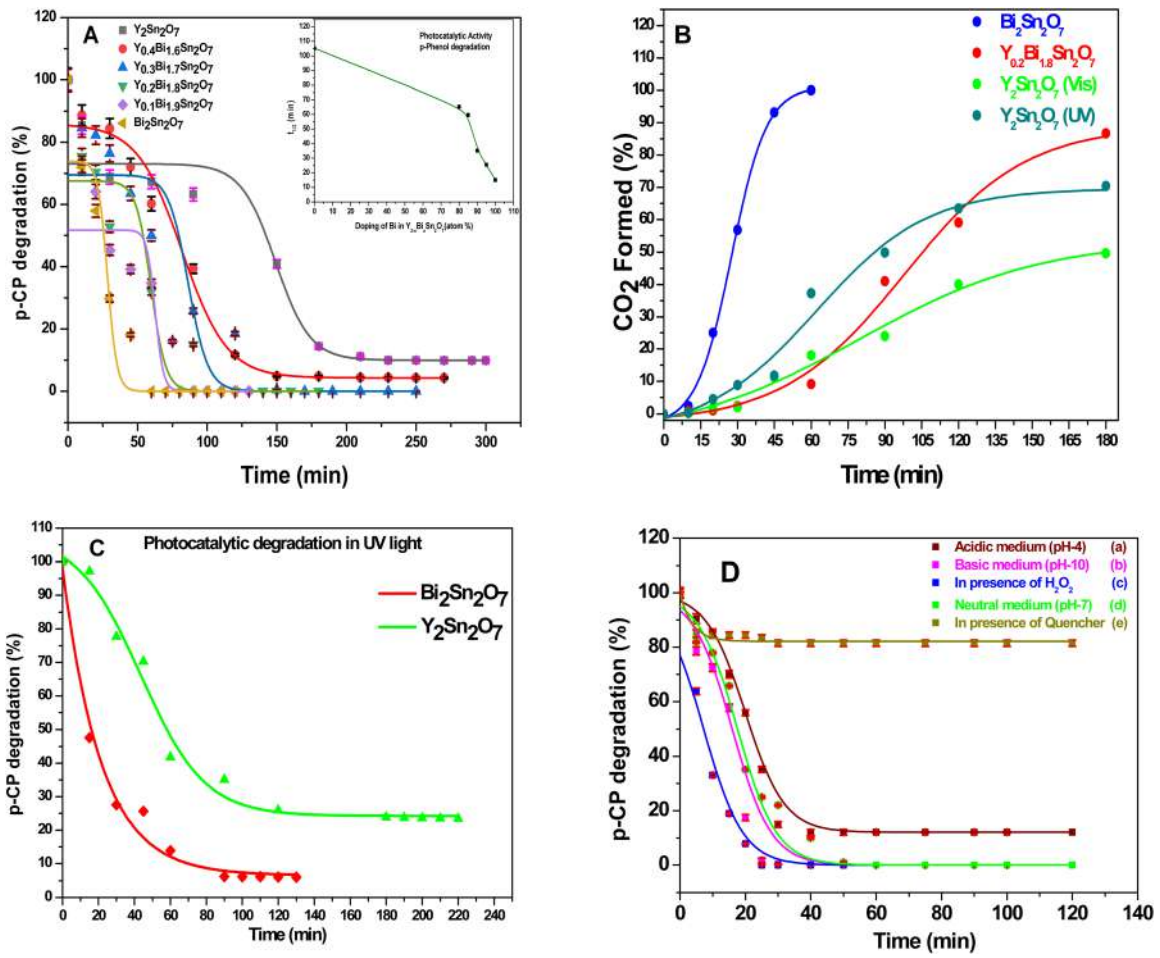

Fig. 9 (A) Photocatalytic degradation of *p*-CP showing the products using different photocatalysts of $Y_{2-x}Bi_xSn_2O_7$ with visible irradiation: (a) YSN; (b) $Y_{0.4}Bi_{1.6}Sn_2O_7$; (c) $Y_{0.3}Bi_{1.7}Sn_2O_7$; (d) $Y_{0.2}Bi_{1.8}Sn_2O_7$; (e) $Y_{0.1}Bi_{1.9}Sn_2O_7$; (f) BSN. Inset shows the plot of $t_{1/2}$ as a function of the Bi dopant in $Y_{2-x}Bi_xSn_2O_7$ (x = 0–100%). (B) Percentage of CO_2 formation (final product) as a function of time using different photocatalysts. (C) Photocatalytic activity of YSN and BSN under UV irradiation. (D) Photocatalytic activity of BSN under different conditions: (a) acidic medium; (b) alkaline medium; (c) presence of H_2O_2; (d) neutral medium; (e) presence of a hole quencher (triethanolamine).

Table 5 A comparative evaluation of advanced catalytic systems for *para*-chlorophenol

Sl no.	Catalyst formulation	Synthetic methodology	*p*-CP conc. (mmol L^{-1})	Irradiation source used	Catalytic performance	References
1	1 wt% Ag(NPs)/$CoFe_2O_4$	Modified co-precipitation method	0.16	$V = 100$ mL, 10 mg catalyst Xe lamp, 40 mW cm^{-2}	90% 4-CP conversion after 120 min	24
2	0.5 at% Pt(IV) or 1.3% Cr(III)-substituted anatase-TiO_2 (mesoporous)	Sol–gel method	—	30 °C-visible light (150 W halogen lamp, λ > 400 nm, 63 mW cm^{-2})	Complete 4-CP conversion after 150 min	25
3	Ag_3PO_4(NPs)/ hydroxyapatite (Hap)	Facile hydrothermal method. Ag_3PO_4 NPs: *in situ* ion exchange	0.08	20 °C, $V = 100$ mL, 150 mg catalyst, visible light (300 W, Xe arc lamp, $\lambda \geq 420$ nm)	70% 4-CP conversion after 90 min	26
4	1.54 wt% Ag–$BiVO_4$/ $InVO_4$	Hydrothermal route at low temperature AgNPs: photo-deposited	0.01	$V = 100$ mL, 50 mg catalyst, visible light (300 W Xe arc lamp, $\lambda > 420$ nm)	60% 4-CP conversion after 120 min	27
5	Au(NPs)/TiO_2–Fe_3O_4 core–shell	Not provided	1 (in 50 : 50 methanol : H_2O)	$V = 100$ mL, 0.1 mg catalyst, visible light (150 W halogen lamp, 350–750 nm), pH = 7	$k_{obs} = 0.108$ mmol h^{-1}	28
6	Cu/Fe-doped CeO_2	Co-precipitation method followed by calcination @ 400 °C	15 ppm	50–200 mg catalyst, 70 W indoor white light (800 × 10 2 lx)	65% degradation efficiency	66
7	BSN (here no co-catalyst was utilized)	Co-precipitation method followed by incineration at 750 °C	3.3 × 10^{-5} mol dm^{-3}	Visible light (234 mW cm^{-2}), $\lambda = 225$ nm, photon flux ~ 6.5 × 10^{14} photons per cm^2 per s, 100 mg catalyst	100% *p*-CP conversion in 60 min	Present work

phenomenon can be attributed to the presence of a higher concentration of oxygen vacancies (O-vacancies) in the BSN materials. These O-vacancies act as deep bulk traps for photo-generated holes (h^+), consequently reducing their lifetime. Further investigation using X-ray photoelectron spectroscopy (XPS) after photocatalytic studies is warranted to elucidate this mechanism in more detail.

Given that these photocatalysts showed impressive activity compared to that in the literature (Table 5), it became imperative to understand the different intermediates formed during the degradation of *p*-CP to understand the photo-oxidation system completely. Therefore, *ex situ* FT-IR was employed to understand the different intermediates formed upon adsorption and reaction over the different photocatalysts.

The effect of different parameters on the photocatalytic activity such as pH and presence of H_2O_2 and hole quencher (as presented in Fig. S.24–S.27 in the ESI†) is plotted as a function of time in Fig. 9D for the BSN photocatalyst. It is quite apparent that a change in pH (both acidic and alkaline) reduced the photocatalytic efficiency [Fig. 9D(a) and (b), respectively]. Similarly, the hole quencher TEA strongly reduced the photocatalytic efficiency (Fig. 9D(c)) illustrating the fact that h^+ plays a definite role in the photo-oxidation of *p*-CP. To further understand the effect of h^+, dynamic experiments were performed accordingly. H_2O_2 showed a definite positive effect, where the kinetics significantly increased during photocatalysis.

3.11. *Ex situ* FT-IR studies

The decrease in absorbance intensity observed using the UV-vis technique provides valuable kinetic data for the photo-degradation of *p*-CP by various catalysts, where providing a comprehensive understanding of the photo-degradation intermediates is crucial for a thorough justification of the reaction mechanism. *Ex situ* FT-IR spectroscopy was employed to identify the different intermediates formed during the oxidative degradation of *p*-CP. As the initial step in any catalytic process, the reactants must adsorb on the catalyst surface. The characteristic bands of pristine *p*-CP are depicted in Fig. S.7,† with detailed descriptions provided in Table S.1 (ESI).† The adsorption behaviour of the *p*-CP solution on the catalyst surface is elaborated in subsequent sections of the ESI (Fig. S.8–S.10).† These findings are further illustrated in Schemes S-1–S-3 (ESI)† and summarized in Scheme 7 (adsorption intermediates). Following adsorption, the reaction intermediates present in the solution for the four representative photocatalysts will be discussed in the subsequent section.

3.11.1. BSN. The different intermediates formed by the BSN photocatalysts are shown in Fig. 10(I). Different vibrational bands as obtained in the solution show the formation of different intermediates by the respective photocatalyst. After 20 min of irradiation, characteristic bands were observed at 3738, 3615, and 3235 cm^{-1}. These bands correspond to the O–H stretching vibration of surface hydroxyl groups (Table 6). The triplet at 2985, 2927, and 2972 cm^{-1} is attributed to the C=C

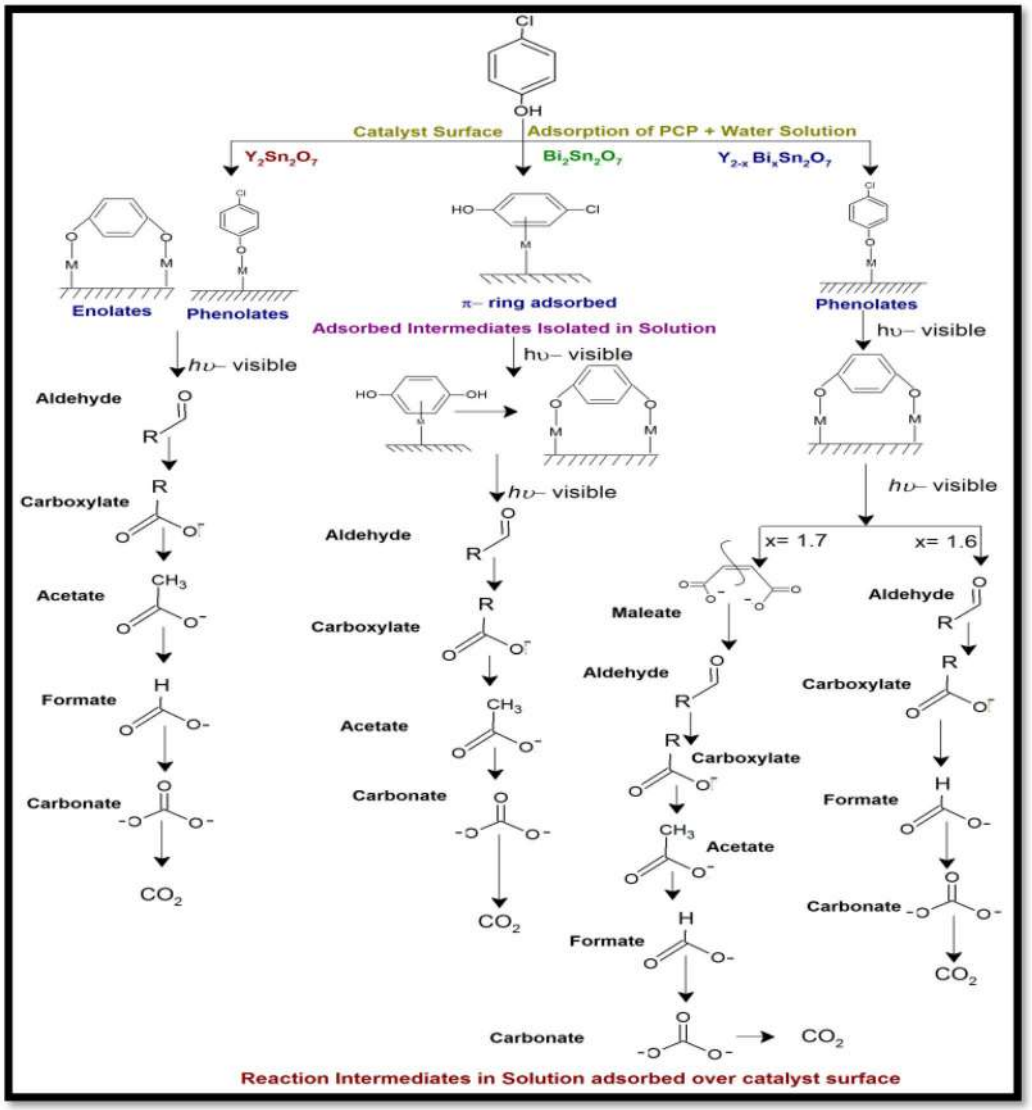

Scheme 7 Reaction mechanism for photo-degradation of *p*-CP over different catalysts.

and C–H stretching modes of adsorbed *o*-dichlorobenzene (*o*-DCB) in its enolic form on the surface of the CeO_2–TiO_2 catalyst, as previously reported by Wang *et al.* (Table 6). However, in the case of BSN, enolates were not formed as the initial adsorbed species (unlike the adsorbed π-ring in *o*-DCB). Instead, they are generated through photo-oxidation.

Fig. 10(I)(A) depicts the bands corresponding to various intermediates detected after 20 min of irradiation at 1753, 1485, 1234, 1096, 962, 621, 509, and 430 cm^{-1}. The bands at 1753 and 430 cm^{-1} are assigned to acetaldehyde.[59,60,63] The remaining bands at 1485, 1234, 962, 621 and 509 cm^{-1} indicate the presence of carboxylate species. Fig. 10(I)(A) and (B) illustrate the changes in intermediate species after 30 min. The intensity of the enolate and surface hydroxyl group bands (Table 6) decreased, suggesting their consumption during the reaction (Scheme 7). New bands appeared at 1368, 1325, 1247, and 1161 cm^{-1}. The bands at 1368 and 1247 cm^{-1} signify carboxylates, while that at 1325 and 1161 cm^{-1} correspond to acetaldehyde (Table 6). After 45 min of irradiation [Fig. 10(I)(A) and (B)], a new band emerged at 1654 cm^{-1}, indicating the formation of carbonates alongside peaks at 1731 and 1485 cm^{-1}. After 60 min of photocatalytic reaction, most of the peaks disappeared, signifying near-complete conversion to CO_2. However, residual peaks persisted at 1714, 1485, 967, and 820 cm^{-1}. The bands at 1714 and 1485 cm^{-1} are attributed to carbonates (Table 6), while that at 967 and 820 cm^{-1} correspond to acetates (Table 6). The proposed reaction pathway for the oxidation of *p*-CP by BSN is depicted in Scheme 7.

3.11.2. $Y_{0.4}Bi_{1.6}Sn_2O_7$. The FT-IR analysis (Fig. 10(II)) revealed the evolution of intermediates during the photo-oxidation of *p*-CP by $Y_{0.4}Bi_{1.6}Sn_2O_7$. After 15 min of irradiation, bands corresponding to surface –OH groups (3663 and 3227 cm^{-1}), formates (1750 and 1494 cm^{-1}), and acetaldehydes (1335, 824, and 500 cm^{-1}) emerged. New bands corresponding to carboxylates (1434 and 1093 cm^{-1}) appeared after 60 min, suggesting a sequential conversion pathway of aldehydes > carboxylates > CO_2 (Scheme 7).

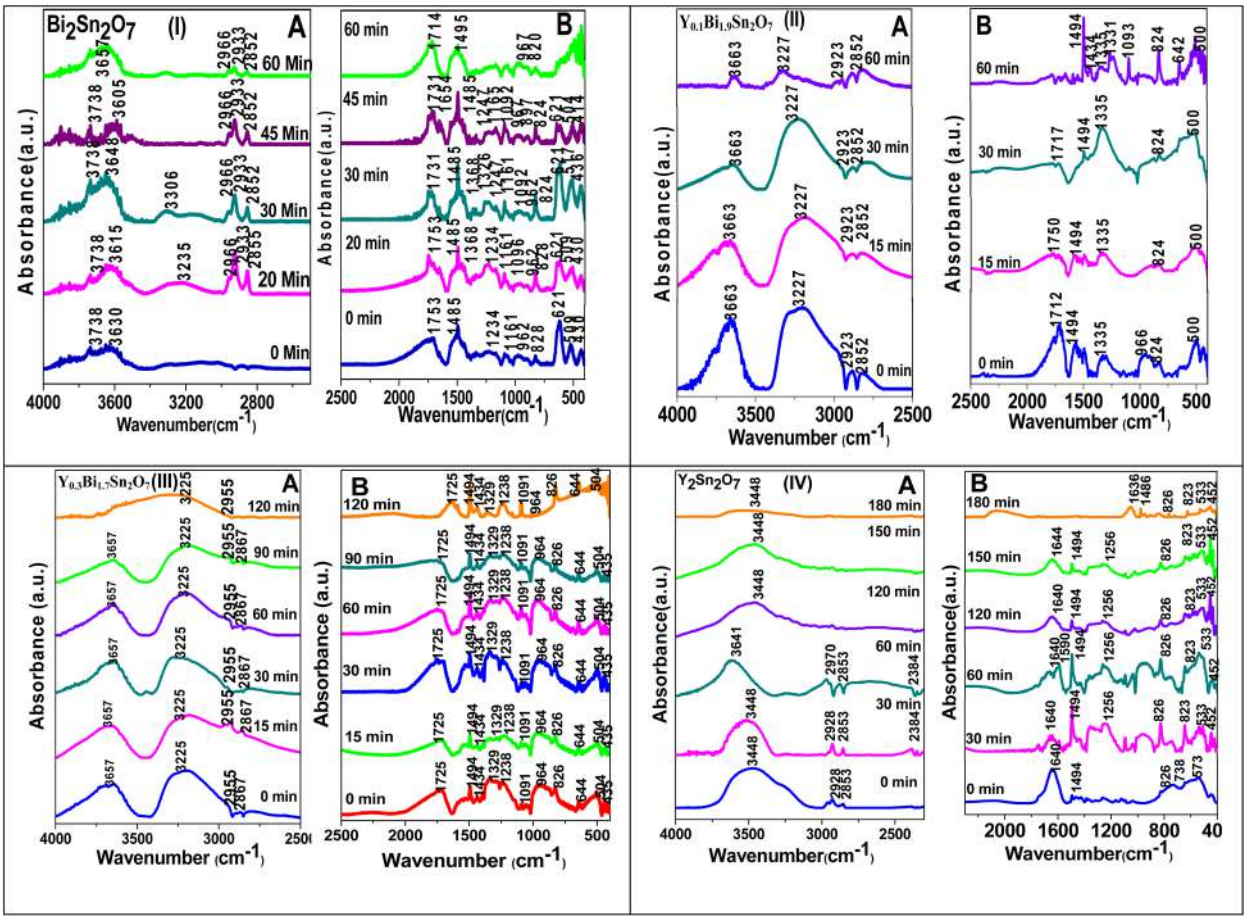

Fig. 10 FT-IR data for reaction of *p*-CP solution over catalysts in the vibrational range of (A) 4000–2600 cm^{-1} and (B) 2600–400 cm^{-1} as a function of time for (I) BSN (0, 20, 30, 45 and 60 min), (II) $Y_{0.1}Bi_{1.9}Sn_2O_7$ (0, 15, 30 and 60 min), (III) $Y_{0.3}Bi_{1.7}Sn_2O_7$ (0, 15, 30, 60, 90 and 120 min) and (IV) YSN (0, 30, 60, 90, 120, 150 and 180 min).

Table 6 Probable assignment of the vibrations bands obtained in *ex situ* FT-IR experiments

Sl no.	Intermediates over CS	Assignment	Bands (cm^{-1})	Requisite CS	Reference
1	Surface –OH groups	O–H stretch	3738, 3615, 3235	—	67
2	Enolates	>C=C<, C–H stretch	2985, 2933, 2855	Y_5	61
3	Carboxylate/acetate	>C=O bend, ν COO^- sym, ν COO^- asym	1640, 1434, 1238, 1093, 966, 500	Y_0, Y_1, Y_3, Y_5	23, 61 and 68–70
4	Acetaldehyde	>C=O bend	1335, 1331, 824	Y_0, Y_1, Y_3, Y_5	71 and 72
5	Carbonate	C–O bend	1731, 1712, 1717, 1651, 1485, 430	Y_0, Y_1, Y_3, Y_5	63
6	Formate	ν C–O bend	1750, 1494	Y_0, Y_1, Y_3, Y_5	63
7	*p*-CP	ν C–Cl bond	642	Y_0, Y_1, Y_3, Y_5	61 and 73

3.11.3. $Y_{0.3}Bi_{1.7}Sn_2O_7$. The FT-IR analysis (Fig. 10(III)) revealed the evolution of the intermediates during the photo-oxidation of *p*-CP by $Y_{0.3}Bi_{1.7}Sn_2O_7$. After 15 min of irradiation, bands corresponding to surface –OH groups (3657 and 3225 cm^{-1}), enolates (2955 and 2867 cm^{-1}), formates (1725 and 1494 cm^{-1}), carboxylates (1238, 1091, 964, and 504 cm^{-1}), and acetaldehydes (826 and 644 cm^{-1}) were observed. After 30 min, new bands signifying carbonates (1715, 1651, 1494, and 430 cm^{-1}) appeared, while the other peaks decreased. These findings (Scheme 7) suggest the sequential conversion pathway of aldehydes > carboxylates > acetates > formates > carbonates > CO_2.

3.11.4. YSN. The FT-IR analysis (Fig. 10(IV)) revealed the evolution of the intermediates during the photo-oxidation of *p*-CP by YSN. After 30 min of irradiation, bands corresponding to surface –OH groups, enolates (2928 and 2853 cm^{-1}), carboxylates (1640, 1494, and 1256 cm^{-1}), acetaldehyde (826 cm^{-1}), and carbonates (434 cm^{-1}) were observed. The enolates differ from that formed with BSN by being adsorbed on the surface of YSN. The band intensities for enolates decreased after 60 min, and

the bands at 1640, 1494, 1256, 826, and 533 cm^{-1} (formates) became prominent by 120 min, and subsequently diminished. These observations suggest the sequential conversion pathway of aldehydes > carboxylates > acetates > formates > carbonates > CO_2 (Scheme 7). Despite being an oxidation reaction, the low valence band potentials of these photocatalysts suggest the possibility of either direct h^+ or $OH^•/H_2O$-mediated processes (h^+ generating $H^•$ and $OH^•$ radicals through water dissociation). The detailed mechanism of intermediate formation will be discussed later. Substantially together with surface –OH groups, no new bands were observed within the short irradiation time.

From 120 min onwards, prominent bands emerged at 1640, 1494, 1256, 826, and 533 cm^{-1}, and subsequently diminished in intensity with extended irradiation. Notably, the bands at 1494 and 533 cm^{-1} are characteristic of formate intermediates.[23] The reaction pathway involves the sequential conversion of aldehydes to carboxylates, then to acetates, followed by oxidation to formates and carbonates, and ultimately in CO_2 generation (Scheme 7).

This section provides an overview of the various intermediates formed during *p*-CP oxidation by the different photocatalysts. It is crucial to recognize that as an oxidation reaction, the process is primarily mediated by photogenerated holes (h^+). Consequently, the valence band potential plays a critical role. As established earlier through the Mott–Schottky analysis, these photocatalysts possess relatively low-lying valence band potentials. This allows the possibility of either the direct h^+ oxidation of *p*-CP or the involvement of hydroxyl radicals $OH^•/H_2O$ in the oxidation process. The initial step in the latter pathway involves h^+-mediated water dissociation to generate H^+ and $OH^•$ radicals. A detailed explanation of how these intermediates are formed will be addressed in a subsequent section.

3.12. Understanding the role of holes (h^+) in the reaction pathway: femtosecond transient absorption (FSTA) measurements

All the photocatalysts possess very low valence band potentials, and thus there is the possibility of direct h^+-mediated *p*-CP oxidation, accompanied by a high likelihood of surface h^+-induced water dissociation, leading to the formation of $H^•$ and $OH^•$ radicals. These radicals are believed to play the primary role in the generation and manipulation of the intermediates observed in the FT-IR analysis.

To elucidate the role of photogenerated holes, femtosecond transient absorption (FSTA) measurements were performed. Owing to its superior catalytic activity, FSTA was performed on BSN dispersed in water. Fig. 11A and B depict the FSTA spectra recorded at various time delays following photoexcitation of the samples with a 350 nm laser pulse. The spectra revealed a broad absorption band in the range of 820 nm to 1100 nm for BSN. Notably, two prominent peaks emerged at approximately 860 nm and 1070 nm within a short time. The decay of the transient species absorbing at 860 nm was found to be slower compared to the species absorbing above 1000 nm. The distinct decay kinetics observed at 860 nm and 1070 nm (Fig. S.20 in ESI†) suggest the presence of two independent species responsible for the absorption at these respective wavelengths. Thus, to identify the nature of these transient species, FSTA experiments were conducted in the presence of a potent hole quencher, triethanolamine (TEA).

As shown in Fig. S.21,† the FSTA spectra in the presence of TEA exhibit its significant influence on the decay kinetics at 1070 nm, with a minimal effect observed at 860 nm. Furthermore, the presence of TEA substantially enhanced the decay at 1070 nm (Fig. S.21†). These findings suggest that the transient species responsible for the absorption above 1000 nm primarily originate from the holes generated during the photoexcitation of the semiconductor catalyst. Conversely, the species absorbing at 860 nm can be attributed to the photogenerated electrons within the catalyst. To investigate the impact of *p*-CP on the kinetics of photogenerated holes, FSTA measurements were performed on BSN in the presence of *p*-CP. As depicted in Fig. 11B, the decay kinetics at 1070 nm remained virtually unchanged upon the introduction of *p*-CP. This result implies that the holes generated by direct photocatalyst excitation do

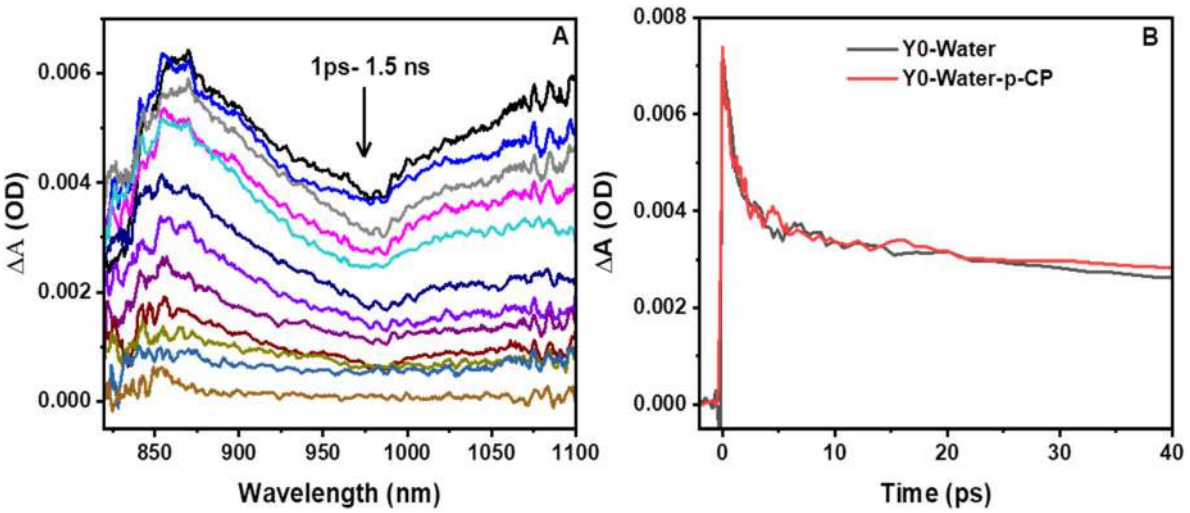

Fig. 11 (A) Transient absorption spectra of BSN dispersed in water at different delay times. (B) Decay kinetics of the transient at 1070 nm for water dispersed solution of BSN in absence and presence of 0.14 M *p*-CP.

not interact directly with *p*-CP. Consequently, it can be inferred that the photogenerated holes first react with water to produce oxidizing radicals, which are subsequently responsible for *p*-CP degradation.

3.13. Post-photo-activity XPS studies

XPS analysis was conducted to elucidate the location of active sites for reactant adsorption and to investigate the post-reaction state of the photocatalysts. Fig. 12A(a) depicts the XPS spectrum of Bi 4f for BSN. The binding energies for Bi $4f_{7/2}$ and Bi $4f_{5/2}$ were observed at 158.2 eV and 163.8 eV, respectively. Notably, a significant downward shift of 0.6 eV was observed compared to the binding energies of the unreacted BSN. Similarly, the Bi 4f peaks for $Y_{0.4}Bi_{1.6}Sn_2O_7$ could be deconvoluted into two peaks at 157.2 eV and 162.4 eV ($4f_{7/2}$) and 168.1 eV and 163.4 eV ($4f_{5/2}$). These peaks exhibit a contrasting shift in binding energy; the 157.2 eV peak showed a 0.6 eV positive shift, while the 168.1 eV peak displayed a 0.6 eV negative shift compared to the corresponding peaks in the pre-reaction catalyst. These observations strongly suggest the preferential adsorption of the reaction intermediates on the Bi-sites of the surface for both the BSN and Bi-substituted YSN photocatalysts.

The Sn 3d spectra show no change in binding energy for BSN after photocatalysis (486 eV and 485.9 eV for $3d_{5/2}$), indicating the minimal involvement of the Sn sites in the reaction. Additionally, no alteration in Sn 3d binding energy was observed with Bi-substitution in the YSN system, consistent with the pre-catalytic observations. As previously described, the O 1s spectrum of BSN exhibits three peaks. However, a significant shift of approximately 2 eV was observed. Interestingly, the O 1s spectrum of Bi-substituted YSN displays an additional peak at 527.7 eV, potentially corresponding to some of the *p*-CP oxidation intermediates, as discussed earlier. Notably, although the two primary O 1s peaks in these pyrochlores show minimal shifts, the intensity of the O-vacancy sites (previously explained) diminished after the photocatalytic reaction.

This decrease in O-vacancy sites suggests their utilization in both the YSN and BSN catalysts. The surface O-vacancies were used more in YSN compared to BSN. These O-vacancies can potentially contribute to the formation of the various intermediates observed on YSN catalysts, as discussed in the preceding section. However, the utilization of O-vacancies for the formation of intermediates will result in a decrease in the partial negative charge of the intermediates, which is not evident in the observed data. Therefore, the primary role of O-vacancies is likely the capture of photogenerated holes (h^+), which consequently reduces the efficiency of the YSN catalysts despite exposure to UV irradiation given that the surface O-vacancies will responsible for the reaction compared to that of the bulk. This phenomenon can be attributed to the lower presence of deep O-vacancy traps in the bulk, as in BSN.

3.14. Discussion

A comprehensive analysis of the interplay between three key variables of band gap, valence band potential, and surface charge and their influence on photocatalytic activity ($t_{1/2}$) is

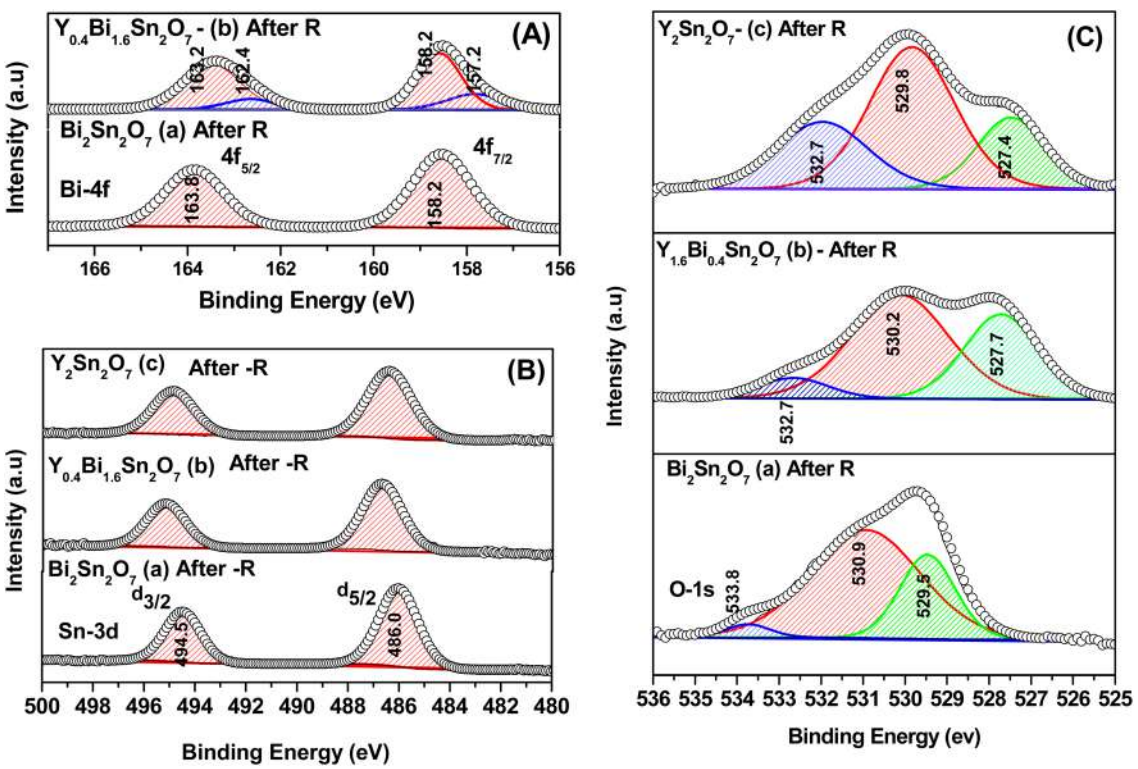

Fig. 12 XPS data of the used catalysts of (A) Bi 4f: (a) BSN; (b) $Y_{0.4}Bi_{1.6}Sn_2O_7$. (B) Sn 3d: (a) BSN; (b) $Y_{04}Bi_{01.6}Sn_2O_7$; (c) YSN. (C) O 1s: (a) BSN; (b) $Y_{0.4}Bi_{1.6}Sn_2O_7$; (c) YSN (after-R-after the catalytic reaction).

presented in Fig. 13. This figure effectively demonstrates how these factors synergistically modulate the photocatalytic degradation of *p*-CP by the Bi-substituted $Y_2Sn_2O_7$ photocatalysts. Notably, $Bi_2Sn_2O_7$ emerged as the most active catalyst, exhibiting a remarkable enhancement in catalytic activity, alongside a concomitant decrease in band gap as the Bi-substitution level increased.

A comparison of $t_{1/2}$ (*t*-half) with the valence band potential calculated from the Mott–Schottky plot is shown in Fig. 13B, while Fig. 13C presents a comparison of $t_{1/2}$ (*t*-half) with the surface charge as calculated from the zeta potential with Bi-substitution in the YSN system.

Greater visible light absorption translates to enhanced photocatalytic activity in these materials. However, another crucial aspect to consider at this stage is the crystal structure. YSN, being a pyrochlore, possesses a more symmetrical structure but exhibits an indirect band gap.

Conversely, BSN, with its tetragonal structure, will inherently possess a lower indirect band gap compared to YSN. Although the band gap of BSN is lower, it has a more indirect band gap nature owing to its higher strain and more phononic coupling compared to YSN. The Raman spectroscopy data, corroborated by the existing literature, suggests significantly higher phonon coupling in BSN and the Bi-substituted YSN due to its structural similarity to BSN. This heightened phonon coupling will inevitably lead to an extended h^+ lifetime in the BSN and Bi-substituted photocatalysts. The calculation of the lattice strain also showed that the BSN lattice has the maximum strain, together with the fact that the substitution of Bi in the YSN lattice created significant lattice strain. This lattice strain on its own with cause an effective increase in phononic coupling and further make the materials show a more indirect band gap nature, which will increase their efficiency as photocatalysts. The effect of surface charge indicated by the zeta potential will impact the adsorption process given that the surface charge induces electrostatic interaction (attraction or repulsion) implemented by the solvated surface over the solvated adsorbate, which is generically explained by the Helmholtz double layer model. According to Fig. 4A, it is obvious that YSN possesses the least negative surface charge, whereas BSN (BSN)

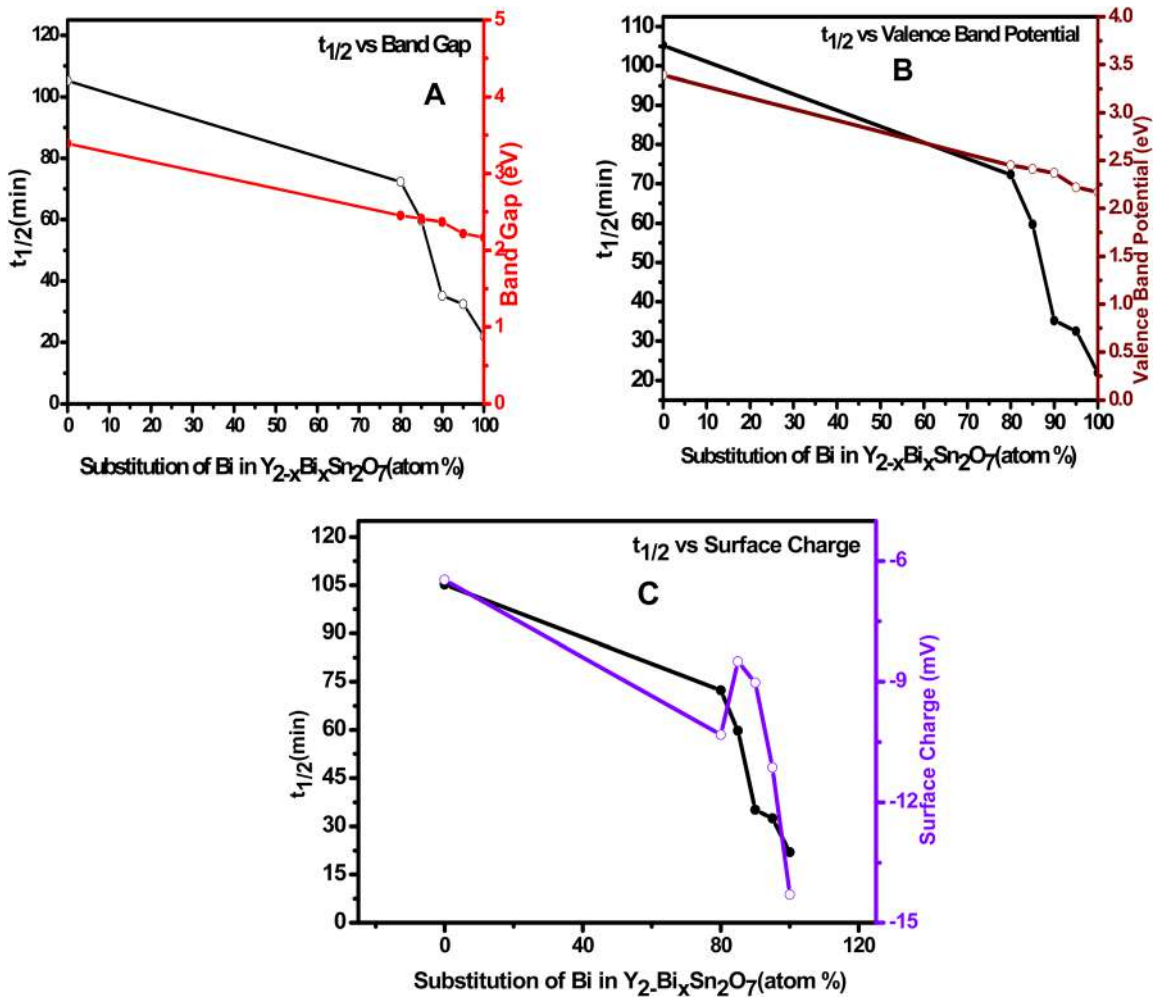

Fig. 13 (A) Comparison of $t_{1/2}$ (*t*-half) with the band gap as calculated from the DRS studies; (B) comparison of $t_{1/2}$ (*t*-half) with valence band potential as calculated from the Mott–Schottky analysis; (C) comparison of $t_{1/2}$ (*t*-half) with surface charge as calculated from zeta potential studies.

has the most negative surface charge. Generally, the surface charge became lesser negative as a function of Bi dopant. The different intermediates formed during the adsorption of *p*-CP on the YSN, BSN and Bi-substituted YSN photocatalysts are elaborated in the ESI† and Scheme 7. The adsorption of *p*-CP on the BSN photocatalysts is mainly affected by the π-ring of chlorophenol. However, in YSN, reactive adsorption occurs *via* the formation of enolates and phenolates, and in Bi-substituted YSN there are mainly phenolates. The enolates are more stabilised over the lower negative YSN surface compared to that of the BSN surface. YSN has a lower surface negative charge, which will stabilise stronger nucleophiles such as enolates and phenolates depending on the sorption energetics, mostly leading to the formation of enolates and phenolates. However, BSN with very a strong negative surface charge does not form enolates but forms more π-ring adduct with the benzene ring of *p*-CP.

However, the formation of the intermediates will not only depend on the surface charge, but also other factors such as the interaction between different intermediates, their dissociation energy to form other intermediates, the conformation of the intermediates, the atomic orbital overlap between intermediates and the catalyst, the ΔG° of the concerned reaction, the energetics of the process, and several others. However, definitely, the adsorbents will play a significant role in the formation of the different intermediates and the surface charge will also affect the intermediates to certain extent. Scheme 7 shows the different intermediates formed in the process to form the final mineralization product of CO_2 over the different catalysts. YSN has a lower surface negative charge, and therefore the intermediates with a higher electron density will be more stable on its surface, which is the opposite in the case of the BSN photocatalyst. This may lead to differential kinetics on these surfaces.

Furthermore, the EXAFS data analysis revealed a strong preference for five-fold coordination by Bi atoms within the YSN system, regardless of their 4f valence orbital. This characteristic persisted despite the Bi substitution. Consequently, the unit cell symmetry of the Bi-substituted YSN systems experienced a further reduction, as observed in the lattice parameters, leading to a more pronounced tetragonal character with an elongated *z*-axis. As inferred from the DRS analysis, these structural characteristics strongly suggest the presence of indirect band gaps for the Bi-substituted YSN materials. These indirect band gaps potentially make the Bi-substituted YSN and BSN superior photocatalysts compared to YSN due to the extended h^+ lifetime facilitated by the significant phonon coupling. This translates to a higher quantum efficiency for these materials. This factor is further emphasised by the fact that the strain in the lattice increased with Bi-substitution. This will lead to an increment in phononic coupling, as observed by Raman spectroscopy, which will increase the lifetime of h^+, thus increasing the oxidative efficiency. The alteration in the surface area of these photocatalysts is shown in Table 1, which shows much less alteration in the surface area with Bi-dopant in the YSN lattice. Given that these materials were calcined at ~750 °C, this will lead to a negligible effect of surface area on photocatalysis. Similarly, Choi *et al.* proposed the formation of charge transfer complexes on TiO_2 with *p*-CP.[74] However, together with the fact that the complete mineralisation of *p*-CP occurred on the present set of catalysts and the surface charge is negative for all the photocatalysts, the formation of CT-complexes is less probabilistic.

Consistent with the observations in Scheme 6, the valence band potential also increased with an increase in Bi-substitution in the YSN system. A higher valence band potential is crucial for the oxidation of *p*-CP into various intermediates during the reaction. As depicted in Fig. 13B, the photocatalysts with a more positive oxidation potential or valence band potential exhibited a superior catalytic performance. Similarly, in the switching experiments, there was definite increment in the photocurrent with Bi in the YSN lattice. This corresponds to more holes being produced, and thereby will also be effective for the photocatalytic property. The photo-oxidation reaction of *p*-CP solution over the Bi-substituted YSN photocatalysts can be understood as a heterogeneous reaction occurring at the solid–liquid interface. This suggests that the formation of intermediates for these photocatalysts may involve the $H^{\bullet}/OH^{\bullet}$ pathway, alongside the hole-mediated (h^+) pathway. Thus, to further understand the effect of $H^{\bullet}$ and $OH^{\bullet}$ radicals in the photocatalytic mineralization, a control experiment was carried out with isopropanol. Given that the reaction is governed by an indirect hole-mediated reaction, the participation of $H^{\bullet}$ and $OH^{\bullet}$ becomes strongly possibility. Xiao and Zhang *et al.* previously showed with *in situ* EPR experiments[75,76] in the presence of the scavenger DMPO (5,5-dimethyl-1-pyrroline-*N*-oxide) how the reaction rate is governed by different radicals. Also, other scavengers have been used, including benzoquinone (BQ), potassium persulfate ($K_2S_2O_8$), *tert*-butyl alcohol (TBA), and Na_2SO_3, which were added to the reaction system to quench superoxide radicals ($^{\bullet}O_2^-$), electrons (e^-), hydroxyl radicals ($^{\bullet}OH$) and holes (h^+), respectively.[77] However, the previous literature shows that alcohol scavenges both $H^{\bullet}$ and $OH^{\bullet}$ together.[78] The control experiment with isopropanol (Fig. S.26B†) showed that the kinetics for the mineralization of *p*-CP were substantially lowered in the presence of the BSN catalysts under similar reaction conditions. This clearly proves the participation of the $H^{\bullet}$ and $OH^{\bullet}$ radicals in the degradation of *p*-CP by the BSN catalyst.

As observed in Scheme 4, the formation and adsorption of most of the intermediates are significantly influenced by ionic interactions, which are dependent on the surface charge. Fig. 13C effectively demonstrates the alteration of surface charge with Bi-substitution. A more negative surface charge hinders the formation of stable adsorbed intermediates, leading to the generation of less stable species, which readily undergo further degradation. Conversely, a more positive surface charge facilitates the formation of stronger and more stable adsorbed intermediates, such as enolates, π-ring intermediates, and phenolates, which typically bind to the surface *via* the oxygen atom or the π-ring moiety of the phenolic structure.

This radical mechanism usually leads to series of radical being formed. However, the positive effect of H_2O_2 (Fig. 9D) on

the photocatalytic reaction rate may possibly indicate that the peroxide radical is one of the important factors in the mineralization of *p*-CP by these photocatalysts. Compared to neutral medium, in both acidic and basic media, the surface charge becomes less negative, which will result in the stabilisation of the intermediates, leading to the lower photodegradation of *p*-CP to CO_2.

The EPR results showed that BSN possessed more bulk O-vacancies compared to YSN; however, the XPS data showed that the surface of YSN possesses a higher amount of O-vacancies compared to BSN, which decreased mostly as a function of Bi-substitution. The XPS results after the photocatalysts were utilised showed the greater usage of O-vacancies by YSN compared to BSN and the Bi-substituted catalysts, given that the BSN and Bi-substituted materials possess more bulk O-vacancies (EPR results). However, the O-vacancies can be used as an h^+ quencher and may result in lower photocatalytic activity for the photocatalyst, which may explain the lower photocatalytic activity of YSN compared to BSN even under UV irradiation. Additionally, the reaction kinetics for BSN was strongly improved by the participation of the $OOH^\bullet$ radical, as observed by the mineralization of *p*-CP by BSN under visible light in the presence of H_2O_2 (Fig. S.26C†). However, the YSN catalyst in the presence of H_2O_2 showed a remarkable decrease in the kinetics of *p*-CP degradation under UV irradiation. This is because it is a secondary hole-mediated process, and under UV there is the strong possibility for the formation of stable H_2O_2 from the $OH^\bullet$ radicals. Given that the H_2O_2 ($OOH^\bullet$) radical affects the BSN photocatalyst positively and the YSN photocatalyst negatively, this can also be a reason for the better performance of the BSN photocatalyst compared to the YSN photocatalyst under UV irradiation.

Among the catalysts, YSN possessed the least negative surface charge, leading to the formation of a relatively stable enolate intermediate. However, the combination of a UV-region band gap and a lower VB oxidation potential makes YSN the least effective photocatalyst in this series due to the challenges associated with degrading the stable enolate intermediate and its limited light absorption capability. In this case several crucial questions emerge, as follows:

(a) Despite the extended h^+ lifetimes in the BSN and Bi-substituted YSN catalysts, the dynamics experiments suggest that *p*-CP degradation is primarily driven by surface h^+, generating $H^\bullet$ and $OH^\bullet$ Intermediates, and not mainly by h^+. Does the extended h^+ lifetime play a decisive role in the reaction kinetics?

(b) Although the surface charge influences the process, the observed intermediate types are largely similar, suggesting the dominant role of radical reactions compared to direct h^+ action, which may have been more susceptible to surface charge effects.

(c) Does the Sn magnetic anisotropy impact photocatalysis? XPS revealed minimal changes in the Sn electron density, while ^{119}Sn NMR showed a significant alteration in the Sn 4d magnetic anisotropy, despite the minimal chemical shift variations. In BSN, its valence band is primarily composed of Bi 6s and Sn 4d. The anisotropic Sn can facilitate electron loss compared to its isotropic counterpart, although the XPS binding energy changes remained minimal, with FWHM variations posing the question of whether they reflect anisotropy?

The highly asymmetric BSN structure compared to the YSN pyrochlore structure raises additional points. Post-catalysis XPS indicated that the Bi electron density was only altered after the reaction, suggesting delocalization during the adsorption and formation of intermediates. In YSN, the dominant role is likely played by the Y electrons, given that the Sn electron density remained constant. The observed changes in the O 1s electron density and O-vacancy states suggest the potential role of O-vacancies as electron traps, potentially influencing the h^+ lifetime in some catalysts. Beyond the direct influence of valence band oxidation, the structural asymmetry of BSN compared to YSN likely plays a role. This asymmetry, as evidenced by the Raman studies, can lead to stronger phonon contributions, impacting the surface transfer kinetics and lifetime of h^+. The BSN structure and Bi-substituted YSN derivatives possess more BiO_5 polyhedra and corner sharing compared to edge sharing in the BSN pyrochlores, potentially affecting the h^+ transfer dynamics.

4. Conclusions

Different Bi-substituted YSN pyrochlores ($Y_{2-x}Bi_xSn_2O_7$, $x = 1.6$ to 2.0) were synthesized and evaluated for their photocatalytic ability in degrading the toxic environmental pollutant *p*-CP. Among them, BSN exhibited the highest activity, demonstrating a clear correlation between Bi-substitution and enhanced photocatalysis. All the catalysts possessed indirect band gaps. The intermediates formed during *p*-CP degradation were identified using *ex situ* FT-IR spectroscopy, allowing the establishment of the degradation mechanism for each photocatalyst, which paves the pathway for future applications. The structure–activity relationships revealed that the band gap, valence band potential, and surface charge significantly influence the photocatalytic properties. The FTAS studies indicated that while these reactions involve photo-oxidation, they are not directly mediated by holes (h^+) but rather by surface H^+, which dissociates water to generate reactive species such as $H^\bullet$ and $OH^\bullet$. The substitution of symmetrical YSN pyrochlores with Bi introduced asymmetry due to the lower coordination number of Bi compared to Y, ultimately leading to an enhanced photocatalytic performance in the BSN structures. Additionally, stronger phononic vibrations, which are more pronounced in the BSN-type structures due to their asymmetry, are likely to extend the lifetime of holes.

Data availability

Data will be available from the authors upon request.

Author contributions

Adarsh Kumar synthesised the photocatalyst samples and performed all the experiments, including the photocatalytic activity and intermediate studies in *ex situ* FT-IR. Deepak Tyagi undertook the XPS experiments. Ravi Kumar performed and

analysed the EXAFS and XANES experiments. Manasi Ghosh undertook the solid state NMR experiments. Balaji P. Mandal synthesised some phase pure photocatalysts and guided Adarsh in the synthesis of the certain catalytic samples. Ahin Roy completed the HRTEM and elemental mapping. Sukhendu Nath performed the FTAS experiment for the BSN catalyst. A. K. Tyagi corrected the manuscript and gave important scientific suggestions to understand the mechanism and catalytic property and helped in conceptualization of the scientific problem. K. Bhattacharyya conceptualized the scientific problem, wrote the manuscript and guided Adarsh on all grounds.

Conflicts of interest

The authors report no conflict of interest.

Acknowledgements

Dr Naveen Kumar and Dr V. Biswanadh of Material Science Division, BARC, for the HR-TEM experiments, Dr A. Gangwar for zeta potential experiment help; Ms. S. Kanth and Dr C. A. Betty of Chemistry Division, BARC, for photo-electrochemical experiments; Shri. S. Saha, RPCD for Raman experiments, Dr Debasis Banerjee of IIT Roorkee for helping with EPR data. A. K. acknowledges Shri Subham Narang from BARC for discussion. A. R. gratefully acknowledges funding from DAE, BRNS, Govt. of India, for the electron microscopy beam time and the SATHI HRTEM facility at IIT Kharagpur for the electron microscopy characterization.

References

1 J. Suntivich, K. J. May, H. A. Gasteiger, J. B. Goodenough and Y. Shao-Horn, *Science*, 2011, **334**, 1383–1385.
2 W. R. Cook Jr and H. Jaffe, *Phys. Rev.*, 1952, **88**, 1426.
3 D. Kulikov and Y. Trushin, *Ferroelectrics*, 2004, **308**, 5–16.
4 G. S. V. Coles, S. E. Bond and G. Williams, *J. Mater. Chem.*, 1994, **4**, 23–27.
5 A. P. Ramirez, A. Hayashi, R. J. Cava, R. Siddharthan and B. S. Shastry, *Nature*, 1999, **399**, 333–335.
6 J. Wu, J. Li, X. Lü, L. Zhang, J. Yao, F. Zhang, F. Huang and F. Xu, *J. Mater. Chem.*, 2010, **20**, 1942–1946.
7 J. M. Longo, P. M. Raccah and J. B. Goodenough, *Mater. Res. Bull.*, 1969, **4**, 191–202.
8 S. A. Luksic, B. J. Riley, M. Schweiger and P. Hrma, *J. Nucl. Mater.*, 2015, **466**, 526–538.
9 S. Murugesan, M. N. Huda, Y. Yan, M. M. Al-Jassim and V. Subramanian, *J. Phys. Chem. C*, 2010, **114**, 10598–10605.
10 M. K. Shamim, G. M. Kale, S. Sardar, D. N. Singh, S. Sharma, A. K. Yadav, S. N. Jha, D. Bhattacharyya and R. J. Choudhary, *Ceram. Int.*, 2024, **50**, 16404–16411.
11 A. Kojima, K. Teshima, Y. Shirai and T. Miyasaka, *J. Am. Chem. Soc.*, 2009, **131**, 6050–6051.
12 B. P. Mandal, K. Bhattacharyya, J. H. Zain, V. Sudarsan, S. Nigam, C. Nayak and A. K. Tyagi, *J. Solid State Chem.*, 2021, **303**, 122472.
13 S. J. Henderson, O. Shebanova, A. L. Hector, P. F. McMillan and M. T. Weller, *Chem. Mater.*, 2007, **19**, 1712–1722.
14 J. W. Lewis, J. L. Payne, I. R. Evans, H. T. Stokes, B. J. Campbell and J. S. O. Evans, *J. Am. Chem. Soc.*, 2016, **138**, 8031–8042.
15 R. D. Shannon, J. D. Bierlein, J. L. Gillson, G. A. Jones and A. W. Sleight, *J. Phys. Chem. Solids*, 1980, **41**, 117–122.
16 J. Wu, F. Huang, X. Lü, P. Chen, D. Wan and F. Xu, *J. Mater. Chem.*, 2011, **21**, 3872–3876.
17 D. Li and J. Xue, *New J. Chem.*, 2015, **39**, 5833–5840.
18 X. Feng, J. Xu, X. Xu, S. Zhang, J. Ma, X. Fang and X. Wang, *ACS Catal.*, 2021, **11**, 12112–12122.
19 M. He, W. Li, J. Xia, L. Xu, J. Di, H. Xu, S. Yin, H. Li and M. Li, *Appl. Surf. Sci.*, 2015, **331**, 170–178.
20 Q. Xing, S. Ren, N. Liu, S. Tong, E. Nkudede, J. Dong, J. Di, M. Ji, S. Yin and J. Xia, *Sol. RRL*, 2024, **8**, 2400099.
21 A. Kumar, Y. Singla, M. Sharma, A. Bhardwaj and V. Krishnan, *Chemosphere*, 2022, **308**, 136212.
22 M. Sharma, A. Kumar and V. Krishnan, *Nanotechnology*, 2022, **33**, 275702.
23 M. Sharma, A. Kumar, D. Gill, S. Jaiswal, A. Patra, S. Bhattacharya and V. Krishnan, *ACS Appl. Mater. Interfaces*, 2023, **15**, 55765–55778.
24 A. Han, H. Zhang, D. Lu, J. Sun, G. K. Chuah and S. Jaenicke, *J. Hazard. Mater.*, 2018, **341**, 83–92.
25 M. Long, Z. E. Ilhan, S. Xia, C. Zhou and B. E. Rittmann, *Water Res.*, 2018, **144**, 134–144.
26 M. Humayun, Z. Hu, A. Khan, W. Cheng, Y. Yuan, Z. Zheng, Q. Fu and W. Luo, *J. Hazard. Mater.*, 2019, **364**, 635–644.
27 G. Jiang, K. Wang, J. Li, W. Fu, Z. Zhang, G. Johnson, X. Lv, Y. Zhang, S. Zhang and F. Dong, *Chem. Eng. J.*, 2018, **348**, 26–34.
28 M. Wang, G. Fang, P. Liu, D. Zhou, C. Ma, D. Zhang and J. Zhan, *Appl. Catal., B*, 2016, **188**, 113–122.
29 S. K. Johnson, L. L. Houk, J. Feng, R. S. Houk and D. C. Johnson, *Environ. Sci. Technol.*, 1999, **33**, 2638–2644.
30 M. F. F. Sze and G. McKay, *Water Res.*, 2012, **46**, 700–710.
31 X.-Q. Lin, Z.-L. Li, B. Liang, H.-L. Zhai, W.-W. Cai, J. Nan and A.-J. Wang, *Water Res.*, 2019, **162**, 236–245.
32 Z. Bian, F. Cao, J. Zhu and H. Li, *Environ. Sci. Technol.*, 2015, **49**, 2418–2424.
33 J. Xu, W. Meng, Y. Zhang, L. Li and C. Guo, *Appl. Catal., B*, 2011, **107**, 355–362.
34 M. M. R. Feijen-Jeurissen, J. J. Jorna, B. E. Nieuwenhuys, G. Sinquin, C. Petit and J.-P. Hindermann, *Catal. Today*, 1999, **54**, 65–79.
35 M. A. Subramanian, G. Aravamudan and G. V. S. Rao, *Prog. Solid State Chem.*, 1983, **15**, 55–143.
36 T. T. Zhang, K. W. Li, J. Zeng, Y. L. Wang, X. M. Song and H. Wang, *J. Phys. Chem. Solids*, 2008, **69**, 2845–2851.
37 I. R. Evans, J. A. K. Howard and J. S. O. Evans, *J. Mater. Chem.*, 2003, **13**, 2098–2103.
38 W. Yan, Y. Zhang and Y. Bi, *Angew. Chem., Int. Ed.*, 2024, **63**, e202316459.
39 I. R. Evans, J. A. K. Howard and J. S. O. Evans, *J. Mater. Chem.*, 2003, **13**, 2098–2103.

40 X. Sun, J. Li, Y. Wang, Y. Zhang and H. Yuan, *Appl. Surf. Sci.*, 2023, **608**, 155228.
41 M. T. Vandenborre, E. Husson, J. P. Chatry and D. Michel, *J. Raman Spectrosc.*, 1983, **14**, 63–71.
42 H. C. Gupta, S. Brown, N. Rani and V. B. Gohel, *J. Raman Spectrosc.*, 2001, **32**, 41–44.
43 N. Garg, K. K. Pandey, C. Murli, K. V. Shanavas, B. P. Mandal, A. K. Tyagi and S. M. Sharma, *Phys. Rev. B: Condens. Matter Mater. Phys.*, 2008, **77**, 214105.
44 M. T. Vandenborre and E. Husson, *J. Solid State Chem.*, 1983, **50**, 362–371.
45 Z. Qu, C. Wan and W. Pan, *Chem. Mater.*, 2007, **19**, 4913–4918.
46 B. P. Mandal, P. S. R. Krishna and A. K. Tyagi, *J. Solid State Chem.*, 2010, **183**, 41–45.
47 S. Brown, H. C. Gupta, J. A. Alonso and M. J. Martinez-Lope, *Phys. Rev. B: Condens. Matter Mater. Phys.*, 2004, **69**, 054434.
48 M. Maczka, J. Hanuza, K. Hermanowicz, A. F. Fuentes, K. Matsuhira and Z. Hiroi, *J. Raman Spectrosc.*, 2008, **39**, 537–544.
49 R. X. Silva, C. W. A. Paschoal, R. M. Almeida, M. C. Castro Jr, A. P. Ayala, J. T. Auletta and M. W. Lufaso, *Vib. Spectrosc.*, 2013, **64**, 172–177.
50 M. Chen, D. B. Tanner and J. C. Nino, *Phys. Rev. B: Condens. Matter Mater. Phys.*, 2005, **72**, 054303.
51 H. Wang, A. Serquis, B. Maiorov, L. Civale, Q. X. Jia, P. N. Arendt, S. R. Foltyn, J. L. MacManus-Driscoll and X. Zhang, *J. Appl. Phys.*, 2006, **100**, 053904.
52 M. Fischer, T. Malcherek, U. Bismayer, P. Blaha and K. Schwarz, *Phys. Rev. B: Condens. Matter Mater. Phys.*, 2008, **78**, 014108.
53 W. Rahim, J. M. Skelton and D. O. Scanlon, *J. Mater. Chem. A*, 2020, **8**, 16405–16420.
54 A. Walsh, G. W. Watson, D. J. Payne, G. Atkinson and R. G. Egdell, *J. Mater. Chem.*, 2006, **16**, 3452–3458.
55 J. Chen, J. Lian, L. M. Wang, R. C. Ewing, R. G. Wang and W. Pan, *Phys. Rev. Lett.*, 2002, **88**, 105901.
56 P. Nachimuthu, S. Thevuthasan, M. H. Engelhard, W. J. Weber, D. K. Shuh, N. M. Hamdan, B. S. Mun, E. M. Adams, D. E. McCready and V. Shutthanandan, *Phys. Rev. B: Condens. Matter Mater. Phys.*, 2004, **70**, 100101.
57 Q. Feng, Q. Wang, Z. Zhang, Y. Xiong, H. Li, Y. Yao, X.-Z. Yuan, M. C. Williams, M. Gu and H. Chen, *Appl. Catal., B*, 2019, **244**, 494–501.
58 J. Xu, Y. Zhu, Z. Liu, X. Teng, H. Gao, Y. Zhao and M. Chen, *Catalysts*, 2023, **13**, 1028.
59 A. Kumar, M. Sharma, S. Sheoran, S. Jaiswal, A. Patra, S. Bhattacharya and V. Krishnan, *Nanoscale*, 2023, **15**, 11667–11680.
60 J. Tian, H. Peng, X. Xu, W. Liu, Y. Ma, X. Wang and X. Yang, *Catal. Sci. Technol.*, 2015, **5**, 2270–2281.
61 N. Y. Kirikova, J. C. Krupa, V. N. Makhov and C. Severac, *J. Electron. Spectrosc. Relat. Phenom.*, 2002, **122**, 85–89.
62 A. A. Yaremchenko, V. V. Kharton, A. V. Kovalevsky, N. M. Lapchuk and E. N. Naumovich, *Mater. Chem. Phys.*, 2000, **63**, 240–250.
63 I. Ahmad, V. Marinova and E. Goovaerts, *Phys. Rev. B: Condens. Matter Mater. Phys.*, 2009, **79**, 033107.
64 S. Gao, R. Wu, M. Sun, M. Guo, D. B. DuBois, S. Chen, H. Ji, C. Wang and Q. Wang, *Appl. Catal., B*, 2023, **324**, 122260.
65 B.-X. Zheng, J.-N. Yuan, P. Su, X. Yan, Q. Chen, M. Yuan and F.-X. Xiao, *J. Mater. Chem. A*, 2025, **13**, 4908–4920.
66 Y.-Q. Yan, Y. Wu, Y.-H. Wu, Z. Weng, S.-J. Liu, Z.-G. Liu, K.-Q. Lu and B. Han, *ChemSusChem*, 2024, e202301778.
67 Y. Gu, X. Jiang, W. Sun, S. Bai, Q. Dai and X. Wang, *ACS Omega*, 2018, **3**, 8460–8470.
68 J. D. Kubicki, L. M. Schroeter, M. J. Itoh, B. N. Nguyen and S. E. Apitz, *Geochim. Cosmochim. Acta*, 1999, **63**, 2709–2725.
69 K. I. Hadjiivanov, D. A. Panayotov, M. Y. Mihaylov, E. Z. Ivanova, K. K. Chakarova, S. M. Andonova and N. L. Drenchev, *Chem. Rev.*, 2020, **121**, 1286–1424.
70 K.-i. Shimizu, H. Kawabata, A. Satsuma and T. Hattori, *J. Phys. Chem. B*, 1999, **103**, 5240–5245.
71 M. Singh, N. Zhou, D. K. Paul and K. J. Klabunde, *J. Catal.*, 2008, **260**, 371–379.
72 J. Raskó and J. Kiss, *Appl. Catal., A*, 2005, **287**, 252–260.
73 M. Czaplicka and B. Kaczmarczyk, *Talanta*, 2006, **70**, 940–949.
74 S. Kim and W. Choi, *J. Phys. Chem. B*, 2005, **109**, 5143–5149.
75 Y.-B. Li and F.-X. Xiao, *Chem. Sci.*, 2025, **16**, 2661–2672.
76 H. Zhang, Y. Gao, S. Meng, Z. Wang, P. Wang, Z. Wang, C. Qiu, S. Chen, B. Weng and Y. M. Zheng, *Adv. Sci.*, 2024, **11**, 2400099.
77 X. Yan, J.-H. Dong, J.-Y. Zheng, Y. Wu and F.-X. Xiao, *Chem. Sci.*, 2024, **15**, 2898–2913.
78 J. Maillard, K. Klehs, C. Rumble, E. Vauthey, M. Heilemann and A. Fürstenberg, *Chem. Sci.*, 2021, **12**, 1352–1362.